ADVANCED MATERIALS

Supporting Information

for *Adv. Mater.*, DOI: 10.1002/adma.202006694

Amphipathic Side Chain of a Conjugated Polymer Optimizes Dopant Location toward Efficient N-Type Organic Thermoelectrics

Jian Liu, Gang Ye, Hinderikus G. O. Potgieser, Marten Koopmans, Selim Sami, Mohamad Insan Nugraha, Diego Rosas Villalva, Hengda Sun, Jingjin Dong, Xuwen Yang, Xinkai Qiu, Chen Yao, Giuseppe Portale, Simone Fabiano, Thomas D. Anthopoulos, Derya Baran, Remco W. A. Havenith, Ryan C. Chiechi,* and L. Jan Anton Koster**

Supporting Information

Amphipathic Side Chain of a Conjugated Polymer Optimizes Dopant Location Towards Efficient N-type Organic Thermoelectrics

Jian Liu, Gang Ye, Hinderikus G.O. Potgieser, Marten Koopmans, Selim Sami, Mohamad Insan Nugraha, Diego Rosas Villalva, Hengda Sun, Jingjin Dong, Xuwen Yang, Xinkai Qiu, Chen Yao, Giuseppe Portale, Simone Fabiano, Thomas D. Anthopoulos, Derya Baran, Remco W. A. Havenith, Ryan C. Chiechi,* and L. Jan Anton Koster**

Dr. J. Liu, Dr. G. Ye, H. G. O. Potgieser, M. Koopmans, S. Sami, J. Dong, X. Yang, X. Qiu, Dr. G. Portale, Dr. R. W. A. Havenith, Prof. R. C. Chiechi, and Prof. L. J. A. Koster
Zernike Institute for Advanced Materials, University of Groningen, Nijenborgh 4, Groningen NL-9747 AG, The Netherlands
E-mail: l.j.a.koster@rug.nl

Dr. G. Ye, S. Sami, X. Qiu, C. Yao, Dr. R. W. A. Havenith, and Prof. R. C. Chiechi
Stratingh Institute for Chemistry, University of Groningen, Nijenborgh 4, Groningen NL-9747 AG, The Netherlands
E-mail: g.ye@rug.nl ; r.c.chiechi@rug.nl

Dr. M. I. Nugraha; D. R. Villalva, Prof. T. D. Anthopoulos, Prof. D. Baran
King Abdullah University of Science and Technology (KAUST), Physical Science and Engineering Division (PSE), KAUST Solar Center (KSC), Thuwal 23955-6900, Saudi Arabia

Dr. H. Sun, Dr. S. Fabiano
Laboratory of Organic Electronics, Department of Science and Technology, Linköping University, SE-601 74 Norrköping, Sweden

Dr. R. W. A. Havenith
Department of Inorganic and Physical Chemistry, Ghent University, Krijgslaan 281-(S3), B-9000 Ghent, Belgium

Table of Contents

Contents

1 Synthesis and characterization of materials

1.1 Instruments of Characterization

^{1}HNMR and ^{13}CNMR were performed on a Varian Unity Plus (400 MHz) instrument at 25 °C, using tetramethylsilane (TMS) as an internal standard. NMR shifts are reported in ppm, relative to the residual protonated solvent signals of $CDCl_3$ (δ= 7.26 ppm) or at the carbon absorption in $CDCl_3$ (δ = 77.23 ppm). Multiplicities are denoted as: singlet (s), doublet (d), triplet (t) and multiplet (m). High-Resolution Mass spectrometry (HRMS) was performed on a JEOL JMS 600 spectrometer. FT-IR spectra were recorded on a Nicolet Nexus FT-IR fitted with a Thermo Scientific Smart iTR sampler. GPC measurements were done on a GPC-PL220 high-temperature GPC/SEC system at 150 °C *vs* polystyrene standards using trichlorobenzene as eluent. The thermal properties of the polymers were determined on a TA Instruments DSC Q20 and a TGA Q50. DSC measurements were executed with two heating−cooling cycles with a scan rate of 20 °C min^{-1}. TGA measurements were done from 20 to 800 °C with a heating rate of 10 °C min^{-1}. Matrix-assisted laser desorption ionization time-of-flight (MALDI-TOF) spectrometry was carried out on a Voyager DE-Pro MALDI-TOF (positive mode, linear detector) with α-cyanohydroxycinnamic acid (5 mg/mL, in 50/50/0.1 water/acetonitrile/trifluoroacetic acid) as the matrix.

1.2 Reagents

All reagents and solvents were commercial and were used as received. Monomer 4,4'-bis(octyloxy)-2,2'-bis(trimethylstannyl)-5,5'-bithiazole (**2Tz**) was purchased from SunaTech. 4,9-dibromo-2,7-di(2,5,8,11-tetraoxanonadecan-19-yl)benzo[lmn][3,8]phenanthroline-1,3,6,8(2H,7H)-tetraone (**NDI2C8TEG**) were synthesized according to literature procedures.[S1] The reference polymer **PNDI2TEG-2Tz** was synthesized according to our previous work [S2] with a slight modification using Pd/Cu co-catalysts.

1.3 Synthetic procedures for monomer NDI2C8TEG and NDI2HexEG.

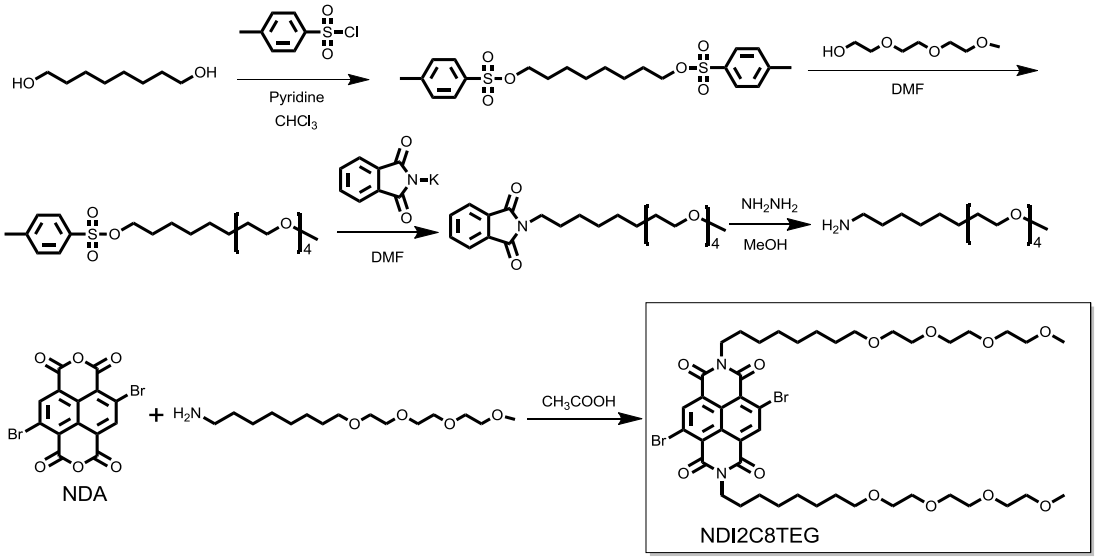

Scheme S1a. The synthetic approach to the NDI-based monomer **NDI2C8TEG.**

4,9-dibromo-2,7-di(2,5,8,11-tetraoxanonadecan-19-yl)benzo[lmn][3,8]phenanthroline-1,3,6,8(2H,7H)-tetraone (**NDI2C8TEG**) was synthesized according to literature procedures.[S1]

NDI2C8TEG: ^{1}HNMR (400 MHz, $CDCl_3$) δ: 8.99 (s, 2H), 4.18 (t, J = 5.6 Hz, 4H), 3.70-3.60 (m, 16H), 3.60-3.50 (m, 8H), 3.44 (t, 4H), 3.37 (s, 6H), 1.80-1.68 (m, 4H), 1.65-1.51 (m, 4H), 1.47-1.27 (m, 16H). ^{13}CNMR (400 MHz, $CDCl_3$) δ: 163.39, 163.37, 141.72, 130.98, 130.37, 127.98, 126.72, 74.58, 74.12, 73.26, 73.23, 73.17, 72.70, 61.70, 44.23, 32.24, 32.00, 31.88, 30.52, 29.67, 28.67. HRMS(ESI) calcd. for $C_{44}H_{65}Br_2N_2O_{12}$ $[M+H]^+$: 973.28783, found: 973.28811; calcd. for $C_{44}H_{65}Br_2N_2O_{12}$ $[M+NH_4]^+$: 990.31438, found: 990.31475.

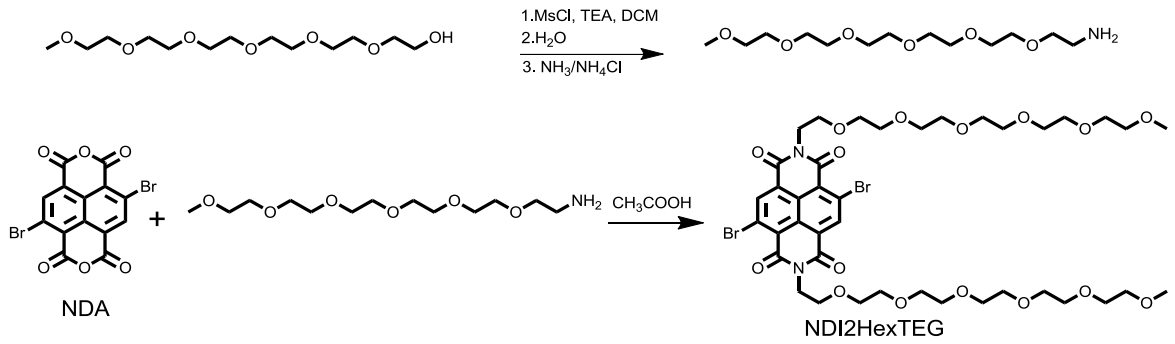

Scheme S1b. The synthetic approach to the NDI-based monomer **NDI2HexEG.**

2,5,8,11,14,17-hexaoxanonadecan-19-amine (HexEGNH2) and 4,9-dibromo-2,7-di(2,5,8,11,14,17-hexaoxanonadecan-19-yl)benzo[lmn][3,8]phenanthroline-1,3,6,8(2H,7H)-tetr-aone (**NDI2HexEG**) was synthesized according to literature procedures [S3-S4].

HexEGNH2: ^{1}HNMR (400 MHz, $CDCl_3$) δ: 3.67-3.59 (m, 18H), 3.55-3.45 (m, 4H), 3.35 (s, 3H), 2.84 (t, J = 5.2 Hz, 2H), 1.63 (br, 2H). ^{13}CNMR (400 MHz, $CDCl_3$) δ: 75.96, 75.93, 74.55, 73.21, 73.19, 73.17, 73.13, 72.91, 61.64, 44.41.

NDI2HexEG: ^{1}HNMR (400 MHz, $CDCl_3$) δ: 8.95 (s, 2H), 4.44 (t, J = 5.6 Hz, 4H), 3.82 (t, J = 6.0 Hz, 4H), 3.69-3.64 (m, 4H), 3.64-3.54 (m, 32H), 3.53-3.46 (m, 4H), 3.34 (s, 6H). ^{13}CNMR (400 MHz, $CDCl_3$) δ: 163.46, 163.37, 141.66, 130.97, 130.41, 127.97, 126.75, 74.55, 73.22, 73.20, 73.18, 73.16, 73.13, 72.69, 70.20, 61.65, 42.65. HRMS(ESI) calcd. for $C_{40}H_{56}Br_2N_2O_{16}Na$ $[M+Na]^+$: 1003.18683, found: 1003.18714.

1.4 Synthetic procedures for conjugated polymer PNDI2C8TEG-2Tz.

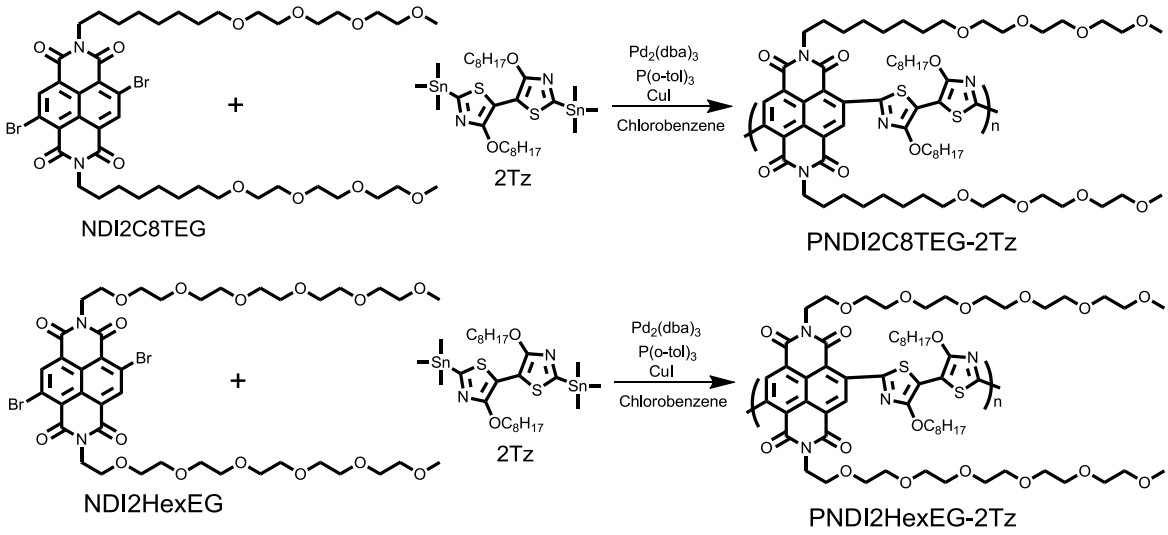

Scheme S2. The synthetic approach to the NDI-based copolymers **PNDI2C8TEG-2Tz** and **PNDI2HexEG-2Tz**.

To a dry three-neck flask, NDI based monomer **NDI2C8TEG** (97 mg, 0.1 mmol) or **NDI2HexEG** (98 mg, 0.1 mmol) and bithiazole monomer **2Tz** (75 mg, 0.1 mmol) were added under N_2 followed by tris(dibenzylideneacetone) dipalladium [$Pd_2(dba)_3$] (8 mg) tri(o-tolyl)phosphine [$P(o\text{-tolyl})_3$] (12 mg), and copper iodide (CuI) (4 mg). The flask and its contents were subjected to 3 pump/purge cycles with N_2 followed by the addition of anhydrous, degassed chlorobenzene (5 mL) via syringe. The reaction mixture was stirred at 110 ^{o}C for three days. After cooling to room temperature, the deeply colored reaction mixture was dropped into 100 mL vigorously stirred methanol (containing 5 mL 12 M

hydrochloride acid). After stirring for 4 hours, the precipitated solid was collected by filtration. The solid polymers were re-dissolved in chloroform and reprecipitated into methanol. After filtration, the polymers were subjected to sequential Soxhlet extraction. The sequential solvents were methanol, hexane, and chloroform. Impurities and low-molecular-weight fractions were removed by methanol and hexane. Finally, the polymer solution in chloroform was concentrated to give the target polymer **PNDI2C8TEG-2Tz** or **PNDI2HexEG-2Tz** as solid.

PNDI2C8TEG-2Tz (110 mg, 89%): ^{1}HNMR (400 MHz, $CDCl_3$) δ: 5.37-2.95 (broad multiplet, 28H), 2.71-0.57 (broad multiplet, 40H). The aromatic protons were hard to be dissolved owing to strong aggregation, only the aliphatic protons assignable to alkyl and glycol groups were observed. IR (cm^{-1}): 668, 691, 722, 764, 791, 899, 949, 1068, 1105, 1177, 1198, 1239, 1299, 1318, 1370, 1443, 1488, 1565, 1645, 1698, 2851, 2918.

PNDI2HexEG-2Tz (120 mg, 96%): ^{1}HNMR (400 MHz, $CDCl_3$) δ: 10.89-8.72 (m, 2H), 5.19-3.03 (broad multiplet, 56H), 2.61-0.72 (broad multiplet, 28H). IR (cm^{-1}): 668, 692, 719, 763, 790, 896, 949, 982, 1065, 1101, 1176, 1209, 1245, 1297, 1314, 1366, 1441, 1487, 1564, 1647, 1698, 2855, 2918.

Molecular weight

Gel permeation chromatography (GPC) is the most and common and facile method to evaluate the molecular weight of conjugated polymer. In our previous work, the molecular weight of **PNDI2TEG-2Tz** was measured by GPC and showed Mn of 26 kg mol−1 at 150 °C using 1,2,4-tricholorobenzene as eluent[S2]. However, the molecular weight of **PNDI2C8TEG-2Tz** was evaluated by GPC at same condition as **PNDI2TEG-2Tz**, giving unbelievable results with the M_n of 0.027 kg mol^{-1} (see Figure S1). This indicates that GPC analytical method meets a problem in this case likely due to very strong aggregation of **PNDI2C8TEG-2Tz**. This phenomenon was also observed in other conjugated polymers with polar glycol side chain [S5]. Therefore, we empolyed the matrix-assisted laser desorption/ionization time-of-flight (MALDI-TOF) mass to detect our polymers molecular weight distribution. The mass spectrum is shown in Figure S2 and the sequences end up with eleven repeating units for PNDI2C8TEG-2Tz, nine repeating units for PNDI2TEG-2Tz, and eleven repeating units for PNDI2HexEG-2Tz, respectively, indicating that the molecular weight of PNDI2C8TEG-2Tz, PNDI2TEG-2Tz, and PNDI2HexEG-2Tz are in the similar range.

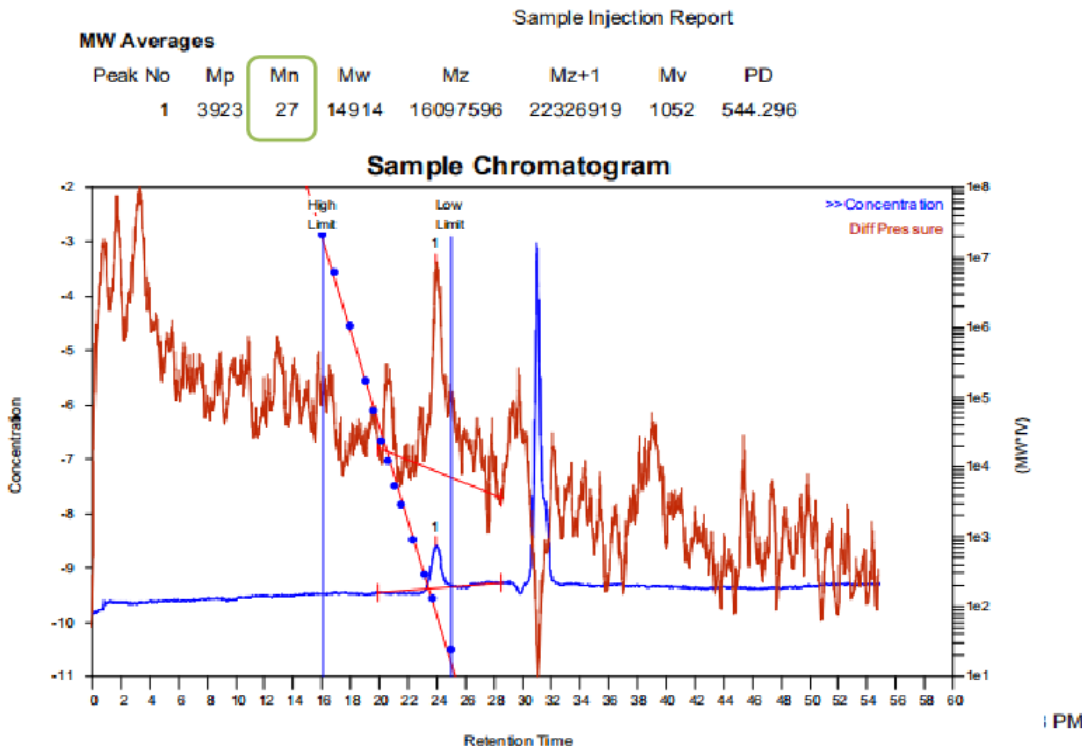

Figure S1. GPC trace of PNDI2C8TEG-2Tz.

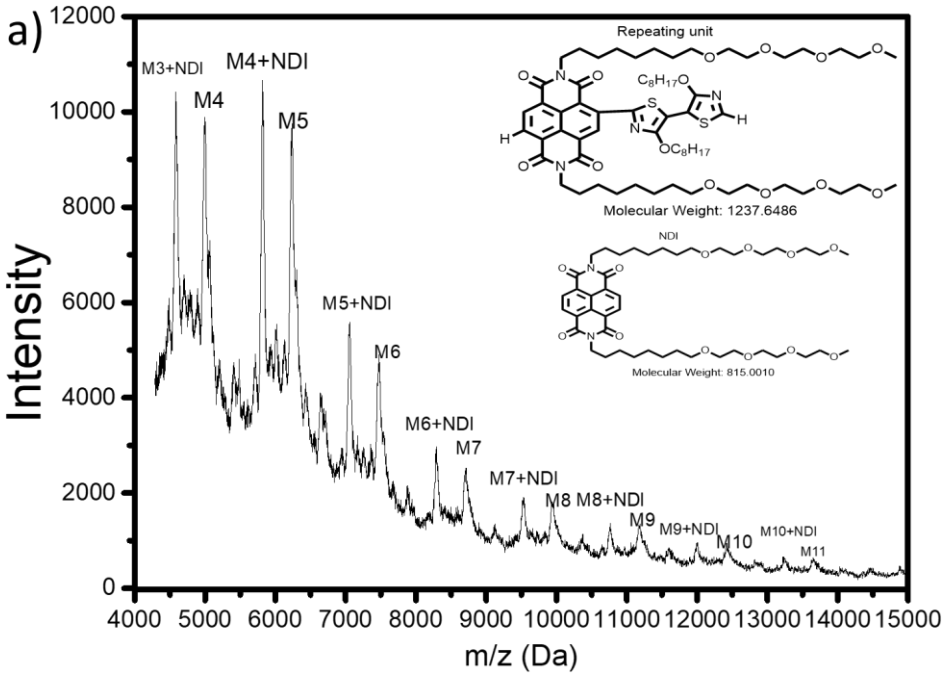

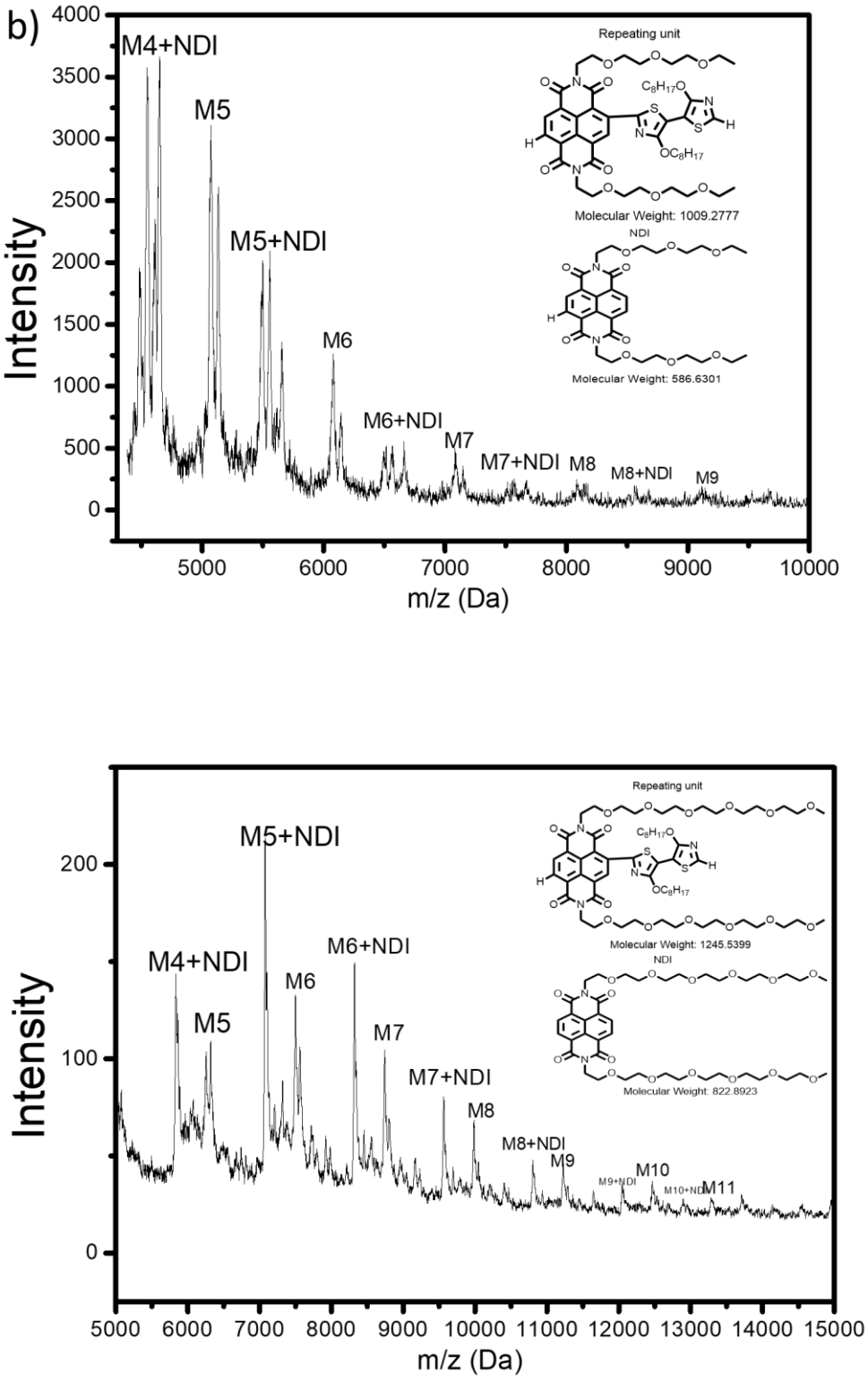

Figure S2. MALDI-TOF-MS spectra of a) PNDI2C8TEG-2Tz, b) PNDI2C8TEG-2Tz, and c) PNDI2HexEG-2Tz.

1.5 Thermal properties of the copolymers.

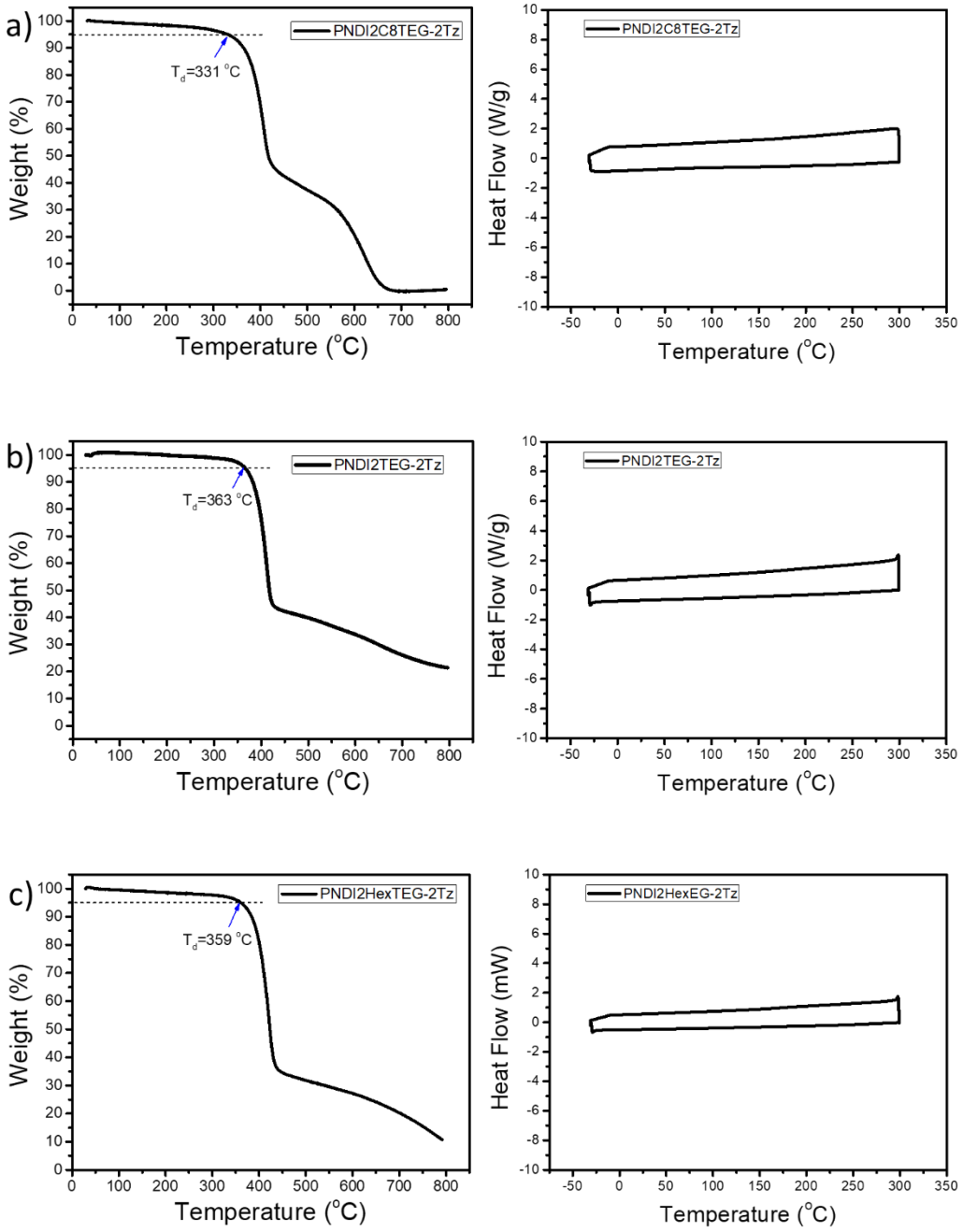

Figure S3. TGA and DSC curves of a) PNDI2 C8TEG-2Tz, b) PNDI2TEG-2Tz, and c) PNDI2HexEG-2Tz.

2 Device fabrication and characterization

2.1 Device fabrication

Clean borosilicate glass substrates were treated with UV-ozone for 20 minutes. The doped films were prepared by spin-coating conjugated polymer solution (7.5 mg/mL in chloroform for PNDI2TEG-2Tz, 5 mg/mL in chloroform for PNDI2C8TEG-2Tz, and 5 mg/ml in chloroform for PNDI2HexTEG-2Tz) mixed with different amounts of dopant solution (10 mg/mL in chloroform) on glass substrates patterned with electrodes in a glovebox with nitrogen atmosphere. The resultant films were annealed at 120 ℃ for 2 hours.

2.2 The measurement of electrical conductivity

For the electrical conductivity measurements of the doped conjugated polymer films, four parallel line-shape Au electrodes with a width (w) of 4.5 mm, which are separated from each other by a distance (L) of 1 mm, were deposited as the bottom contact before spin-coating. 4-point-probe measurements were performed by Keithley 4200scs semiconductor analyzer to measure the electrical conductivity of the samples in an N_2-controlled environment. The electrical conductivity was calculated with $= \frac{I}{V} \cdot \frac{L}{w \cdot d}$, with L (1 mm), w (4.5 mm), and d as the length, width and height of the channel respectively. Each electrical conductivity value was obtained by averaging six points.

2.3 Seebeck coefficient measurement

The Seebeck coefficient of doped conjugated polymer thin-film samples were measured in a home-built setup reported previously [S6]. Two Peltier devices are placed with a gap of 6 mm in parallel on a heat sink. The temperatures of two Peltier devices can be controlled by two independent PID controllers The two rectangular Au electrodes (width: 3 mm and length: 5 mm) are deposited on thin film coated glass substrate with a distance of 8 mm. The samples are mounted on the Peltier devices as shown and thermal paste is used for good thermal contact. Two T-type thermocouples (127 μm from Omega) are used as probes for simultaneous temperature and thermal voltage. Note that a silver paste (ELECTRODAG 1415) was used to connect thermocouple probes with the Au electrodes. The cold junctions of the thermocouples are connected to a printable circuit board (PCB), whose temperature is measured by Pt100 sensor. A Keithley 2000 mounted

scanner card is used for signal recording with a delay time of 100 ms. The system is controlled by Labview software. In order to remove the thermal voltage (∆V) shifting, A 'quasi-static' approach by slowly changing temperature difference (∆T) is used to extract the Seebeck coefficient.

3 Characterization of thin films properties

The thicknesses of all the films were measured by ellipsometry and Bruker Dektak. The thicknesses of PND2TEG-2Tz film and PND2C8TEG-2Tz film are determined to be 64 ± 4 nm and 53 ± 3 nm by the Bruker Dektak. The effect of the doping on the thickness of the film samples is within the measurement error. AFM topographical images were recorded in the tapping mode using a Bruker MultiMode 8 microscope with TESP probes. Peak force quantitative nanomechanical mapping (PFQNM) AFM measurements were performed on a Bruker AFM multimode MMAFM-2 model. Freshly prepared spin coated films of PNDI2TEG-2Tz and PNDI2C8TEG-2Tz were characterized by AFM. Measurements of height, adhesion, deformation and DMT modulus were performed in PFQNM mode. The samples were contacted with a silicon nitride tip with a nominal radius of 2 nm (ScanAsyst-Air, Bruker, resonant frequency 70 kHz, spring constant 0.4 N m^{-1}). The deflection sensitivity, spring constant of the cantilever and tip radius were calibrated both before and after measurements. Samples were scanned at 5 um at a rate of 0.8 Hz with a peak force setpoint of 0.32 nN. UV-vis-NIR spectra of pristine and doped copolymer thin films coated on glass substrates, which were sealed in an air-tight sample holder in N_2-filled glove-box, were recorded on Shimadzu UV 3600. Cyclic voltammetry (CV) was carried out with a Autolab PGSTAT100 potentiostat in a three-electrode configuration where the working electrode was glassy carbon electrode, the counter electrode was a platinum wire, and the pseudo-reference was an Ag/AgCl wire that was calibrated against ferrocene (Fc/Fc^+). Cyclic voltammograms for the D-A copolymer films deposited on the glassy carbon working electrode in $CHCN_3$ solution containing Bu_4NPF_6 (0.1 mol L^{-1}) electrolyte at a scanning rate of 100 mV s^{-1}.

3.1 Mobility measurement by the field-effect transistors

The field effect transistors (FET) based on pristine donor-acceptor conjugated copolymers were fabricated with a bottom contact and top gate geometry. The heavily doped silicon substrates with 230 nm thermal oxide insulator were purchased from

Fraunhofer Institute for photonic microsystems (IPMS). The channel length and width are defined by interdigitated Au electrodes as 20 μm and 10 mm, respectively. After cleaning the substrates by sequential ultrasonication in acetone and isopropanol for 20 minutes, the active layers were prepared by spin-coating directly on substrates from chloroform solution (5 mg/mL), followed by thermal annealing at 120 °C for 1 h. Poly(methyl methacrylate) (PMMA) dielectric layer was prepared on top of the active layer by a spin-coating process. 100 nm Al was deposited with a mask as the top electrode. The transistor devices were tested on a probe station sitting in N_2-filed glovebox with data recorded by Keithley 4200scs semiconductor analyzer.

3.2 Field-effect Seebeck coefficient measurement

To measure the gate modulated Seebeck coefficient of the conjugated polymer, a micropatterned device structure with on chip heater is fabricated with a photolithography method, demonstrated in Scheme S3. The bottom electrodes are patterned from Cr(3 nm)/Au(30 nm) bilayer, having wire width of 10 μm. When certain voltages are applied on the heater wire, a temperature difference dT is created between the source and drain wire as the heat is transported through the channel. The temperature at source or drain side could be detected by its resistance, following the equations below [S7]:

$T_{hot\text{-}end}=300+(R_{hot}-R_{hot@300K})/TCR$

$T_{cold\text{-}end}=300+(R_{cold}-R_{cold@300K})/TCR$

$dT= T_{hot\text{-}end} -T_{cold\text{-}end}$

where TCR is the temperature coefficient of resistance, which can be calibrated with precisely controlled external heat source, in our device it is found to be 1.21.

The polymer channel is spin-coated from 5 mg/mL solution in chloroform followed by 120 ℃ annealing for 1 hour, resulting in a film thickness of about 30nm. After photolithographic patterning of the conjugated polymer channel, a 900 nm PMMA dielectric layer is spin-coated on top followed by 80 ℃ annealing for 2 hours. At last, 50 nm Al gate electrode is evaporated through a shadow mask. All the processing steps except the photolithography part are done in N_2-filled glovebox. Seebeck measurement and basic FET characterizations are done in vacuum probe stations, with the help of Keithley 4200 FET station.

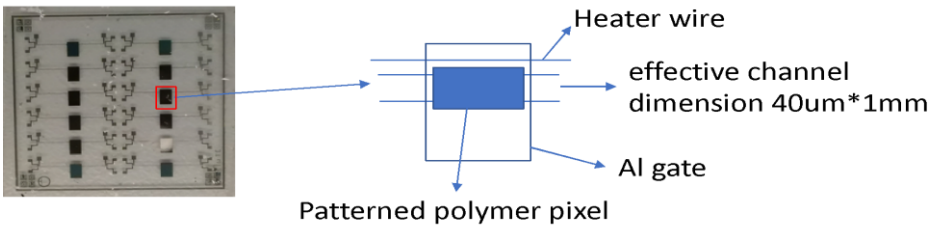

Scheme S3. The picture of the device for measuring field-effect Seebeck coefficient.

3.3 EPR measurement

Thin-film samples were prepared on a flexible substrate and sealed in EPR tubes within a nitrogen-filled glove-box. A continuous-wave Bruker ELEXSYS E500 electron paramagnetic resonance (EPR) spectrometer operating at the X band (microwave frequency, 9.7–9.9 GHz), equipped with a super high Q resonator (ER 4122 SHQ) was used to record all EPR spectra. The spectra were measured using the same conditions for all samples. Bruker Xenon software (Bruker BioSpin, Rheinstetten, Germany) was used to collect the data, post-processing and spin counting.

3.4 Metal-insulator-semiconductor (MIS) devices

The MIS devices have an architecture of ITO/insulator/doped donor-acceptor copolymer films/Al). For ion gel solution preparation, 251 mg PVDF-HFP was dissolved in 3.17 mL cyclohexanone stirred at 70 ℃ at 1000 rpm overnight add 91 mg [EMIM][TFSI] into the solution and stirred 55 ℃ until 1 hour before spin-coating. Ion gel solution was spin-coating on clean ITO substrates to form 150-300 nm insulator layer followed by annealing at 140 ℃ for 6 h. Various doped PNDI2TEG-2Tz and PNDI2C8TEG-2Tz films were prepared by spin-coating with a thickness of around 120 nm on top of insulators. The capacitance-voltage (C_p-V_d) measurement was conducted at a frequency of 10 Hz for ion gel based devices for AC bias. The carrier density (n) was extracted by Mott-Schottky analysis:

$$n = \frac{2}{e\varepsilon_0\varepsilon_r \frac{\partial C_P^{-2}}{\partial V}} \qquad \text{(S2)}$$

Where e, ε_0, and ε_r are elementary charge, dielectric constant of vacuum and relative dielectric constant of active layer, respectively. ε_r=3 was used for both doped layers.

3.5 2D GIWAXS

Grazing incidence wide-angle X-ray scattering (GIWAXS) measurements were performed using a MINA X-ray scattering instrument built on a Cu rotating anode source (λ=1.5413 Å). 2D patterns were collected using a Vantec500 detector (1024x1024 pixel array with pixel size 136x136 microns) located 93 mm (for PNDI2C2TEG-2Tz) and 123 mm (for PNDI2C8TEG-2Tz) away from the sample. The conjugated polymer based films were placed in reflection geometry at certain incident angles α_i with respect to the direct beam using a Huber goniometer. GIWAXS patterns were acquired using incident angles from 0.25° to 2° in order to probe the thin film structure at different X-ray penetration depths. The direct beam center position on the detector and the sample-to-detector distance were calibrated using the diffraction rings from standard silver behenate and Al_2O_3 powders. All the necessary corrections for the GIWAXS geometry were applied to the raw patterns using the GIXGUI Matlab toolbox. The reshaped GIWAXS patterns, taking into account the inaccessible part in reciprocal space (wedge-shaped corrected patterns), are presented as a function of the vertical and parallel scattering vectors q_z and q_r. The scattering vector coordinates for the GIWAXS geometry are given by:

$$q_x = \frac{2\pi}{\lambda}\left(\cos\left(2\theta_f\right) cos\ \cos\left(\alpha_f\right) - \cos(\alpha_i)\right);\ q_y = \frac{2\pi}{\lambda}\left(sin\ sin\left(2\theta_f\right)\ cos\ cos\left(\alpha_f\right)\right);\ q_z = \frac{2\pi}{\lambda}\left(sin\ sin\left(\alpha_i\right)\ + sin(\alpha_f)\right) \quad \text{(S3)}$$

where $2\theta_f$ is the scattering angle in the horizontal direction and α_f is the exit angle in the vertical direction. The parallel component of the scattering vector is thus calculated as $q_r = \sqrt{q_x^2 + q_y^2}$.

3.6 Figures of experimental and simulated results

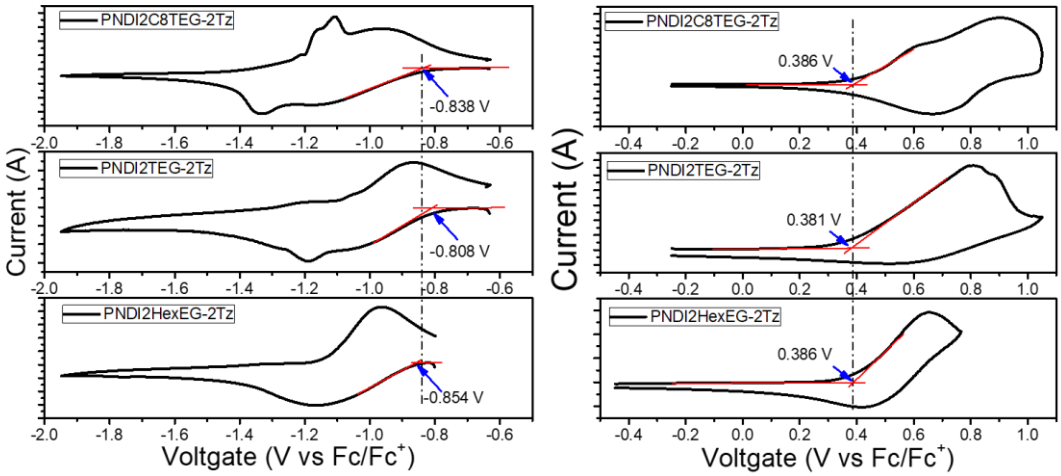

Figure S4. Cyclic voltammograms of the conjugated polymers (PNDI2C8TEG-2Tz, PNDI2TEG-2Tz, and PNDI2HexEG-2Tz) thin films deposited on the glass carbon working electrode.

Table S1. Energy level of of PNDI2C8TEG-2Tz, PNDI2C8TEG-2Tz, and PNDI2HexEG-2Tz.

Energy Level	PNDI2C8TEG-2TZ	PNDI2TEG-2TZ	PNDI2HexTEG-2TZ
LUMO [a]	-4.26 eV	-4.29 eV	-4.25 eV
HOMO [b]	-5.49 eV	-5.48 eV	-5.49 eV

a LUMO= -(5.10 + $E^{red.}_{onset}$) eV

b HOMO= -(5.10 + $E^{ox.}_{onset}$) eV

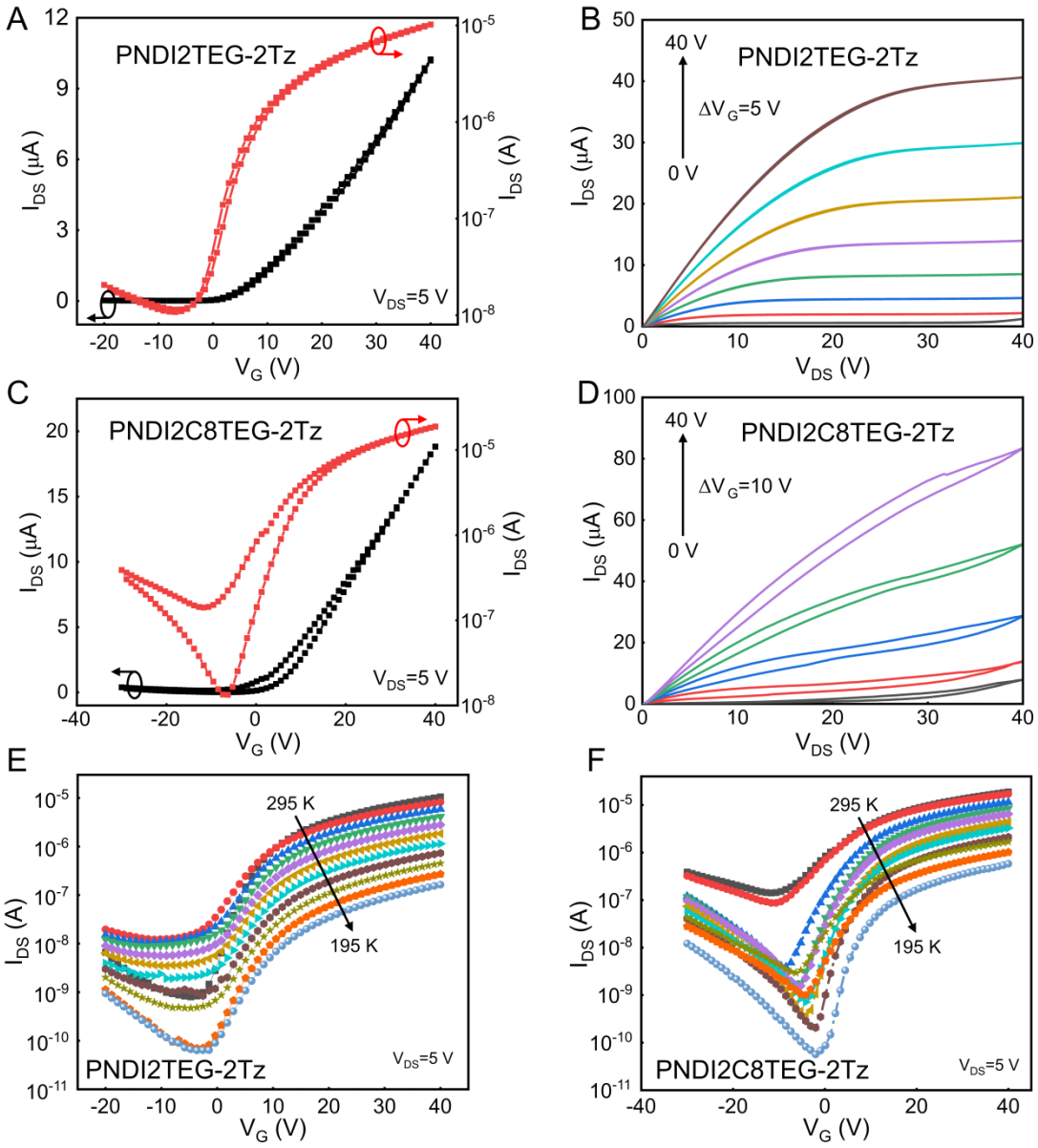

Figure S5. Top-gate/bottom-contact OTFT transfer (A and C) and output (B and D) characteristics of PNDI2TEG-2Tz and PNDI2C8TEG-2Tz based devices; the temperature dependent transfer characteristics of PNDI2TEG-2Tz (E) and PNDI2C8TEG-2Tz (F) based devices.

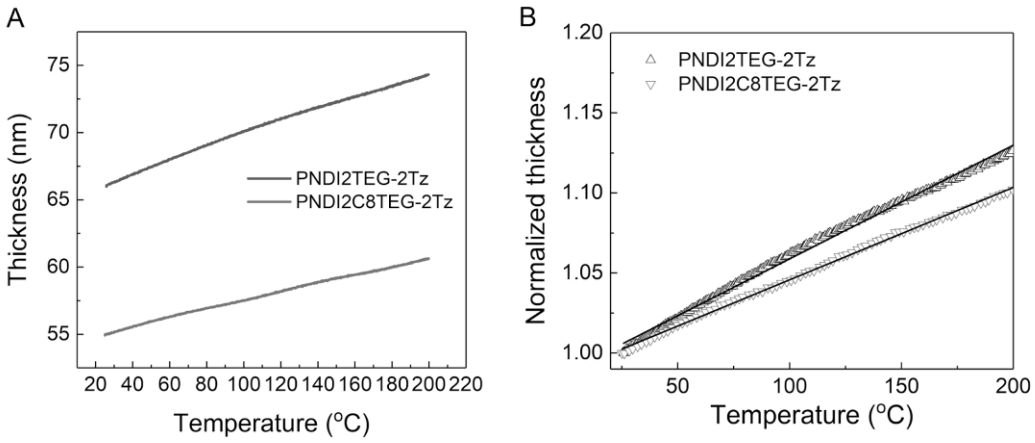

Figure S6. The thermal expansion (A: thickness variation; B: the change in the normalized thickness to the original value at RT) of the pristine PNDI2TEG-2Tz and PNDI2C8TEG-2Tz thin films. The solid black lines represent the linear fits to the thermal expansion plots on the right hand.

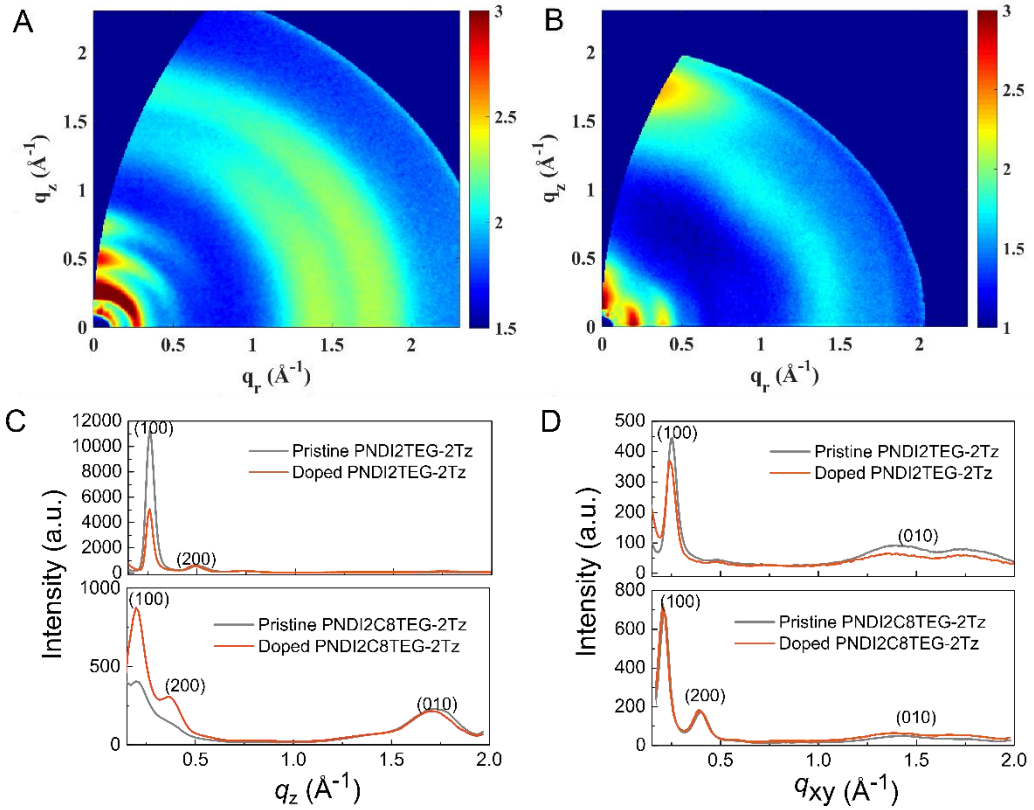

Figure S7. The 2D GIWAXS patterns of the pristine PNDI2TEG-2Tz (A) and PNDI2C8TEG-2Tz (B) film; (C and D) linecuts of the pristine and 5 wt%-doped copolymers.

4 Molecular dynamics simulations

Molecular dynamics (MD) simulations were performed with force fields generated with the Q-Force procedure [S8-S9]. Each unit cell contained 12 PNDI2TEG-2Tz or PNDI2C8TEG-2Tz monomers, one neutral n-DMBI, and one cationic n-DMBI. This ratio was based on the experimental dopant concentration. Periodic boundary conditions were applied in three directions. The MD simulations were carried out in several steps to maximize sampling; starting at a high-temperature and a low mass density (liquid-like system) and gradually relaxing the system to normal conditions, while allowing the morphology to form. The force field files corresponding to all employed molecules, the initial configurations and all final morphologies for both systems are provided in two files named "md_files_pndi2c8teg-2tz.tar" and "md_files_pndi2teg-2tz.tar" in the Supporting Information.

The following 8 MD simulation steps were carried out in series (484 times for PNDI2C8TEG-2Tz and 476 times for PNDI2TEG-2Tz) on starting configurations with unit cell dimensions of 6 x 6 x Z nm^3 (Z=3.5 nm for PNDI2C8TEG-2Tz and Z=2.3 nm for PNDI2TEG-2Tz) : 1) 1500 K, 1 ns, 150 bar, with flat bottom potential (FBP) and chain restraint, and z-dimension fixed at the starting size ; 2) gradual cooldown from 1500 to 1000 K over 2.5 ns, followed by a 0.5 ns relaxation, 150 bar, with FBP and chain restraint, and z-dimension fixed at the starting size; 3) 1000 K, 1.5 ns, 150 bar, with FBP and chain restraint, and z-dimension relaxed; 4) 1000 K, 1.5 ns, 1 bar, with FBP and chain restraint; 5) gradual cooldown from 1000 to 500 K over 2 ns, followed by a 1 ns relaxation, 1 bar, with FBP and chain restraint; ; 6) 500 K, 2 ns, 1 bar, with FBP, and chain restraint relaxed; 7) 500 K, 2 ns, 1 bar, FBP relaxed; 8) gradual cooldown from 500 to 298 K over 2 ns, followed by a 2 ns relaxation. These steps amount to a total of 18 ns simulation time per each run. FBP refers to the use of a flat bottom potential used to keep the backbone of the molecules on Z = 0 with a flat bottom of 0.3 nm with the aim of preserving a lamellar packing inferred from the GIWAXS measurements. Chain restraint refers to a harmonic potential used to keep the side chain extended in the first few steps of the simulation in order to prevent chain coiling in the high temperature, low density "gas phase". Weak coupling schemes [S10] were used in steps to maintain pressure, in an anisotropic way and with a compressibility of $5 \cdot 10^{-6}$ per bar, and temperature. Coupling parameters were 0.1 ps and 0.5 ps for the temperature and pressure, respectively. For non-bonded interactions a cutoff of 1 nm was used for both Lennard-Jones and Coulomb

interactions and the Particle Mesh Ewald (PME) method [S11] was used in both cases to treat the interactions beyond this cut-off. The simulations were performed using the GROMACS 2018 software package [S12]. π–π stacking distances obtained from the MD simulations are given in Figure S8. The final unit cell parameters in Z corresponds to 2.12 ± 0.11 and 2.80 ± 0.15 for PNDI2TEG-2Tz and PNDI2C8TEG-2Tz, respectively.

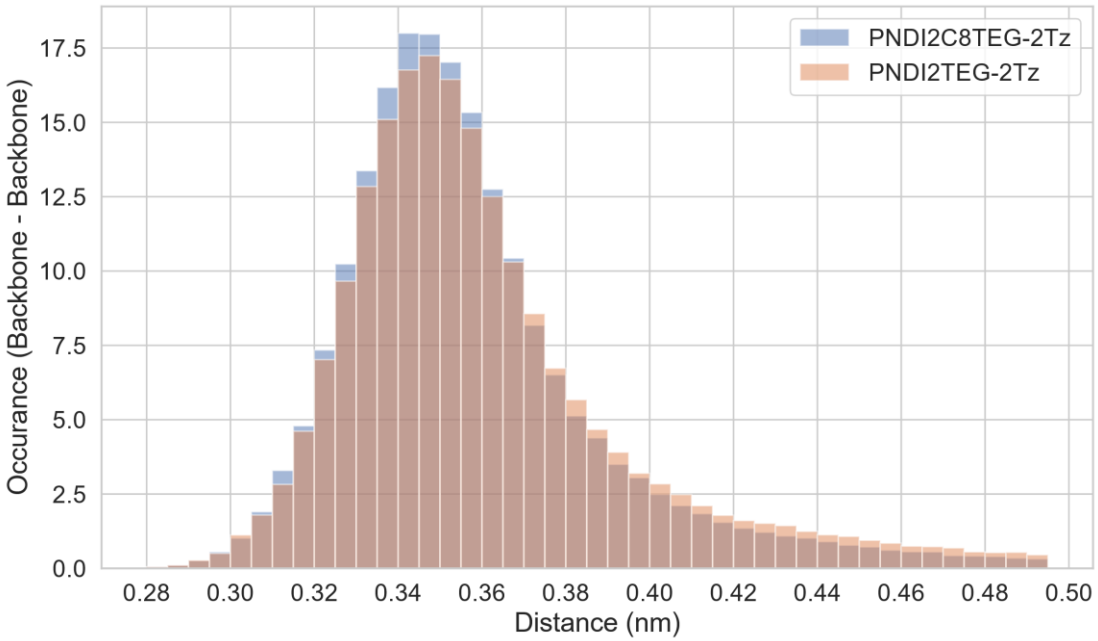

Figure S8 Histogram of the distance of each atom on a backbone to the nearest atom of another backbone. The distributions for the two molecules are almost identical, with the darker color corresponding to the overlap between the two.

Two sample videos are provided as the Supporting Information that highlights the formation of the morphologies during the 8 MD steps described above. The first one (dopant.mp4) demonstrates the sampling of preferential dopant sites, where the dopants can be seen traveling to the backbone and return multiple times. The second one (backbone.mp4) shows formation of the π-π stacking of the backbone. For both videos: dark gray=backbone, white=alkyl units, light red=ethylene glycol units, green=n-DMBI(+), purple=n-DMBI(0).

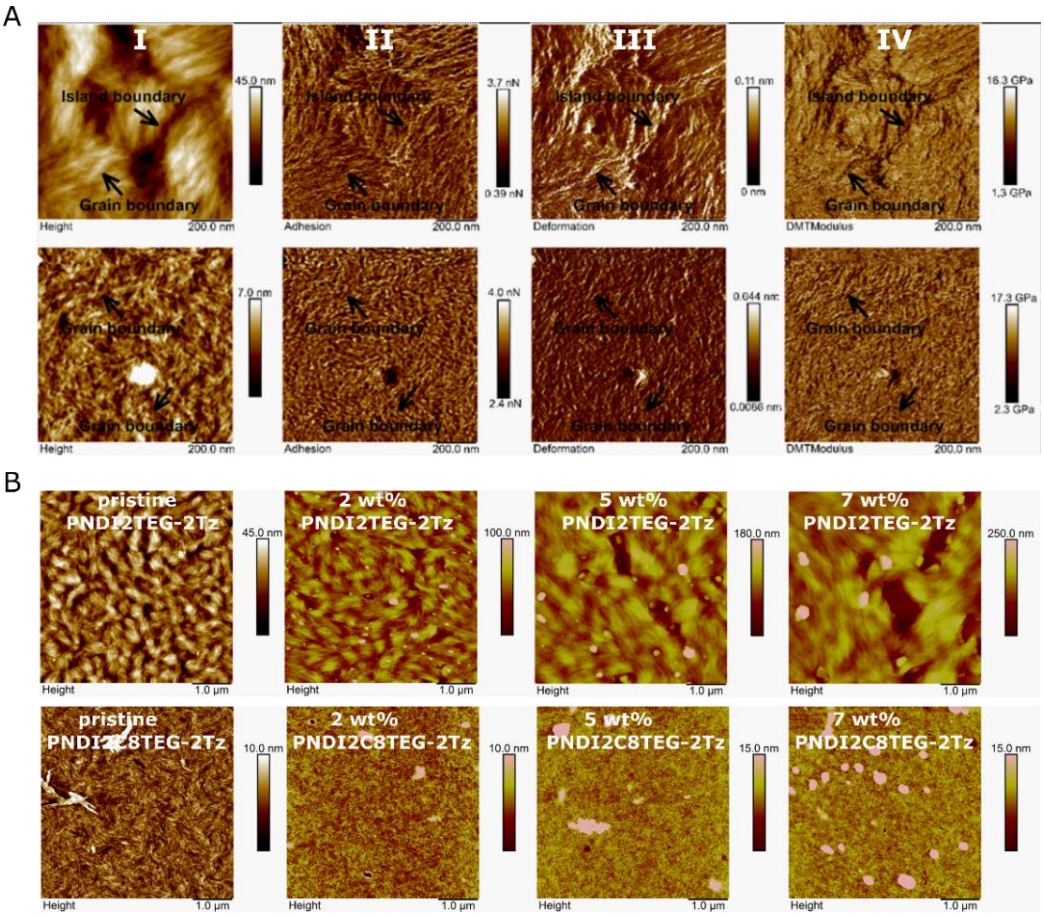

Figure S9. (A) Characterization of the mechanical properties of the polymer films. (I) The AFM height images of the spin coated films of PNDI2TEG-2Tz (top) and PNDI2C8TEG-2Tz (bottom); (II) the adhesion between the AFM tip and the spin coated films of PNDI2TEG-2Tz (top) and PNDI2C8TEG-2Tz (bottom); (III) the deformation generated by the AFM tip on the spin coated films of PNDI2TEG-2Tz (top) and PNDI2C8TEG-2Tz (bottom); (IV) the Derjaguin-Muller-Toporov moduli characterized on the spin coated films of PNDI2TEG-2Tz (top) and PNDI2C8TEG-2Tz (bottom). The arrows indicate the formation of grain boundaries and island boundaries on the polymer films. (B) topographic AFM morphology images of pristine and various doped PNDI2TEG-2Tz (the top panel) and PNDI2C8TEG-2Tz (the bottom panel) films.

We characterized the mechanical properties of the PNDI2TEG-2Tz and PNDI2C8TEG-2Tz films by atomic force microscopy (AFM). The interactions between the AFM tip and the organic films were quantified and translated into morphology, adhesion, deformation, elastic modulus within one scan (Figure S9A). Features such as island boundaries and grain boundaries in the spin coated films, which are challenging to identify from surface

morphology (Figure S9A-I), can be visualized by their distinctly different mechanical properties compared to the bulk of the polymers (Figure S9A II-IV). We observed both grain boundaries (narrow boundaries with low adhesion and high deformation) and island boundaries (broad boundaries with low adhesion and high deformation) in the spin coated films of PNDI2TEG-2Tz; while in the films of PNDI2C8TEG-2Tz, only grain boundaries were observed. Though we were unable to resolve each polymer chain, the clear orientation of grain boundaries in the films of PNDI2TEG-2Tz suggests the formation of semi-crystalline structure from the polymer. The absence of such feature in the spin coated films of PNDI2C8TEG-2Tz may corresponds to the formation of amorphous phase. Both films yield similar elastic moduli calculated from the Derjaguin-Muller-Toporov (DMT) model, with 11.3 GPa found for PNDI2TEG-2Tz and 12.3 GPa found for PNDI2C8TEG-2Tz.

Figure S10. Optical images of pristine and 5 wt%-doped copolymers (PNDI2TEG-2Tz and PNDI2C8TEG-2Tz) stored in ambient (21 ^{o}C and humility: 46%) for different periods (fresh samples, 14 days, and 27 days).

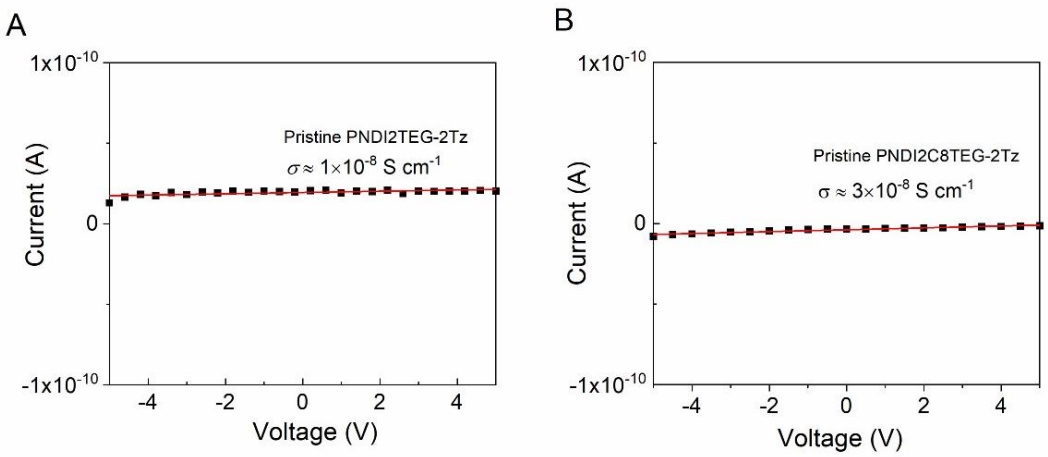

Figure S11. The measured I/V curves (by two point probes) for (A) pristine PNDI2TEG-2Tz and (B) pristine PNDI2C8TEg-2Tz film.

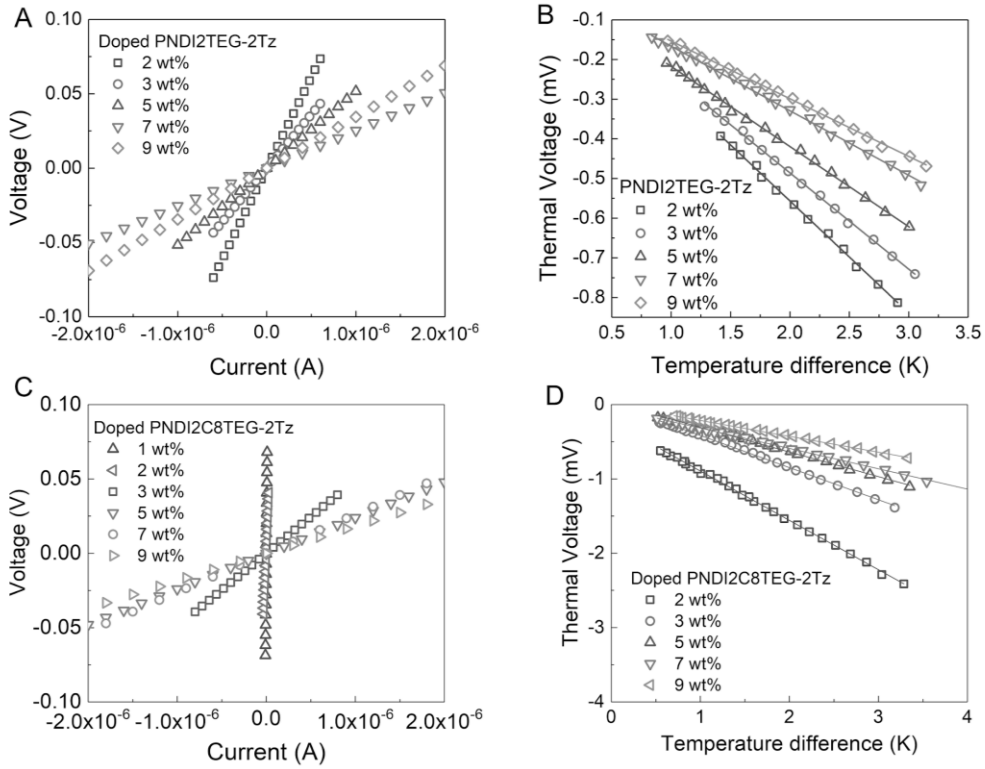

Figure S12. The measured I/V curves for the doped PNDI2TEG-2Tz (A) and doped PNDI2C8TEg-2Tz (C) films at various doping concentrations (2-9 wt%); the measured thermal voltage (ΔV) - temperature difference (ΔT) curves for the corresponding doped PNDI2TEG-2Tz (B) and PNDI2C8TEG-2Tz (D) films. The Seebeck coefficients are extracted from the slopes obtained by linear fits to the ΔV-ΔT plot.

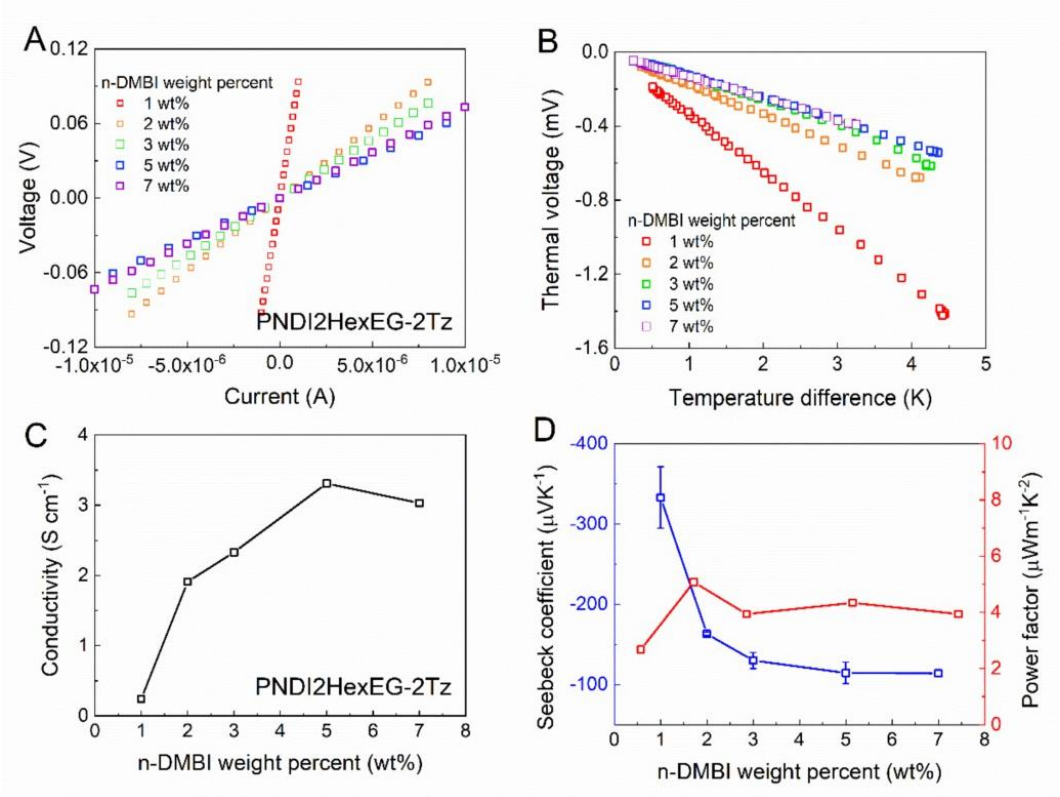

Figure S13. (A) The measured I/V curves (by four point probes) for the doped PNDI2HexEG-2Tz films with various n-DMBI loading; (B) the measured thermal voltage (ΔV) - temperature difference (ΔT) curves for the corresponding doped PNDI2HexEG-2Tz films; (C) the electrical conductivity and (D) Seebeck coefficient and power factor of various doped PNDI2HexEG-2Tz films.

Table S2. Summary of thermoelectric parameters for n-type thermoelectric materials based on molecularly doped conjuagted polymers.

Material	Dopant	Conductivity [S/cm]	Seebeck coefficient [μVK^{-1}]	Power factor [$\mu Wm^{-1}K^{-2}$]	Ref.
PNDIC82TEG-2Tz	n-DMBI	**1.6±0.1**	**-326±31**	**16.5±1.2**	This work
PNDI2TEG-2Tz	n-DMBI	**1.36**	**-167±13**	**3.8±0.6**	This work
PNDIHexEG-2Tz	n-DMBI	**1.9**	**-163 ± 2**	**5.1**	This work
PNDI2TEG-2T	n-DMBI	7.0×10^{-4}	-57.2±3.1	2.3×10^{-4}	S2
PNDI2TEG-2Tz	n-DMBI	1.8±0.1	-159±8	4.6	S2
N2200	n-DMBI	8×10^{-3}	-850	0.6	S13
TEG-N2200	n-DMBI	0.17	-153	0.4	S14
p(gNDI-gT2)	n-DMBI	0.3	-93	0.4	S15
P(NDI2OD-Tz2)	TDAE	0.06	-447	1.5	S16
PNDTI-BBT-DP	n-DMBI	5	−169	14	S17
P(EO-NDIT2)	N-DiPrBI	0.02	-331	0.11	S18
BBL	TDAE	1.2	-60	0.43	S19
FBDPPV	n-DMBI	14	-140	28	S20
ClBDPPV	TBAF	0.62	-99±9	0.63	S21
P(PzDPP-CT2)	n-DMBI	8.4	-261	57.3	S22
pNB-TzDP	n-DMBI	11.6	-214	53.4	S23
FBDPPV	TAM	21	-156	51	S24

5 The Kinetic Monte Carlo simulation

Modeling of the Seebeck coefficient and conductivity

To qualitatively model the effect of the spacer length on the Seebeck Coefficient and conductivity, Kinetic Monte Carlo (KMC) simulations were employed. KMC simulations are a powerful tool for studying the steady-state transport of polarons in disordered organic semiconductors. To perform these KMC simulations the Excimontec simulation software was used, developed by Mike Heiber [S25].

Lattice

In the model the disordered semiconductor is represented by a cubic lattice with a lattice dimension of 70, corresponding to 70^3 lattice sites which can be occupied by charge carriers. The lattice constant *a*, which is the distance between lattice points, was taken to be 1nm. The disorder is taken into account by assigning random energies to each lattice site according to a Gaussian distribution, whose width (σ = 0.0776 eV) is proportional to the degree of disorder. Furthermore, the inclusion of stationary dopants at random lattice sites is realized by altering the energies of the surrounding lattice sites according to an electrostatic potential. It is assumed that the mobile charge carrier density equals the dopant density. The intrinsic disorder and dopant potentials remain unchanged throughout the simulation. The energetic contribution of mobile charge carriers to the potential energy of the lattice sites is recalculated after every hopping event. In this way, carrier-carrier and carrier-dopant interactions are accounted for. As such, the lattice represents the potential energy landscape through which mobile charge carriers navigate. A full list of all parameters can be found at the end of this section in Table S2.

Algorithm

The BKL[S26] algorithm is used to model charge transport. Charge transport in the model is hopping. At the start of the simulation charge carriers are put at the lowest energy positions of the energetic landscape and all possible hop events are listed and their hop rates calculated. The hop rates implemented are of the Miller-Abrahams [S27] type and are defined by the expression:

$$\nu_{ij} = \{\nu_0 exp\left(-2\alpha R_{ij} - \frac{E_j - E_i}{k_b T}\right) \quad for\ E_j > E_i\ \nu_0 exp\left(-2\alpha R_{ij}\right)\ for\ E_j < E_i$$

where ν_0 is the attempt-to-hop frequency, α the inverse localization radius, R_{ij} the inter-site distance, E_j and E_i the energies of site j and i respectively, k_b the Boltzmann constant and T the temperature. After the list is created a hopping event is randomly selected and executed.

Although the selection of an event is random, the probability of selection is proportional to the hop rate of that event. After a hopping event is executed, the energetic values of surrounding lattice sites are updated (with respect to the new position of the mobile charge carrier) within a certain recalculation radius. Subsequently all possible events (in this case within the same recalculation radius) for neighboring charge carriers are recalculated. After this the next event is selected and the process repeats a set amount of times.

Equilibration

While at the start of the simulation the mobile charge carriers are placed at the energetic minima of the base energetic landscape, it does not correspond to the lowest energy configuration. That is because the presence of the mobile charge carriers is yet to be taken into account. Hence the system needs to cycle through a sufficient amount of events to achieve a steady state. The agreement between the actual temperature and the set temperature was chosen as a criterion for equilibration, with the number of events chosen accordingly. The actual temperature was obtained by dividing the ODOS by the DOS and subsequently fitting the Fermi-Dirac distribution.

Modelling of the spacer length

The effect of increasing the spacer length is considered to increase the distance Rmin between dopant and charge carrier. This is factored into the simulation by restricting the Coulomb potential of a dopant such that V(Rmin) becomes the new V(0) with respect to a lattice site (see figure S14). For the data in the paper three such values of Rmin were used: 0.7, 0.9 and 1.1nm.

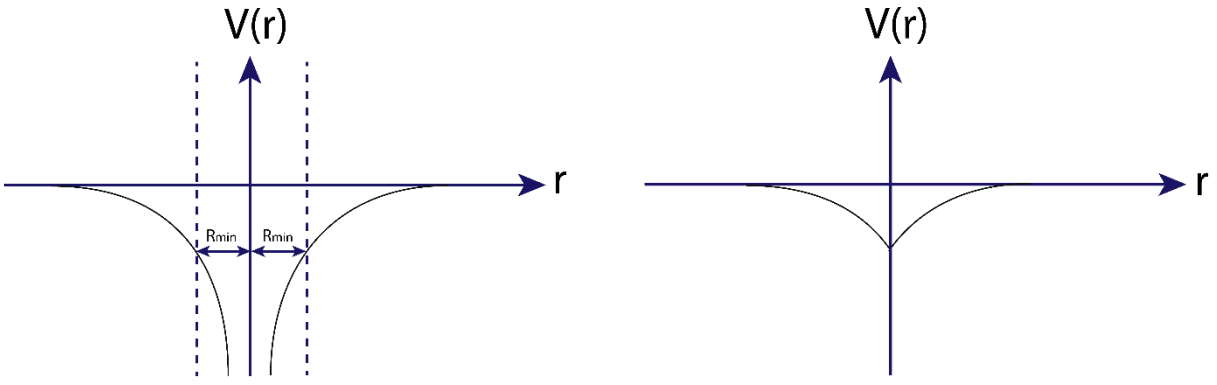

Figure S14: Illustration of how spacer length is implemented in the model. Rmin is the minimum distance from the backbone to the dopant; hence the dopant potential at this distance replaces V(0) as the minimum since dopant and carrier are not assumed to get closer. The inner part of the potential is effectively 'cut out'.

Determination of conductivity and Seebeck coefficient

Each datapoint in the Seebeck vs. conductivity graphs is the average of 30 separate simulations. The conductivity was output directly by the simulation and for the calculation of the Seebeck Coefficient the following expression [S28] was used:

$$S = \frac{k_b}{q}\int_{-\infty}^{\infty} -\frac{(E - E_F)}{k_b T}\frac{\sigma(E)}{\sigma} = -\frac{1}{qT}(E_{tr} - E_F)$$

Determination of percentage of bound carriers

The minimum distance from a carrier to a dopant was determined for all charge carriers. A distance of 0 was then assumed to signify that a charge carrier is 'bound' to the dopant, for in that case they are at the same lattice point and cannot get any closer in the simulation. Using this criterion, the percentage of bound charge carriers was calculated.

6 Parameter list

Table S3: List of Parameters

Parameter	**Value**	**Description**
Nxyz	70	Lattice dimension
a	1 nm	Lattice spacing
T	300 K	Temperature
ε_r	4	Relative dielectric constant
E	100.000 V/cm	Electric field
ν_0	1e12	Attempt to hop frequency
Rr	6.93 nm	Recalculation radius
Cc	6.93 nm	Coulomb cut-off radius
Nsims	30	Number of simulations
α	1 nm	Delocalization length

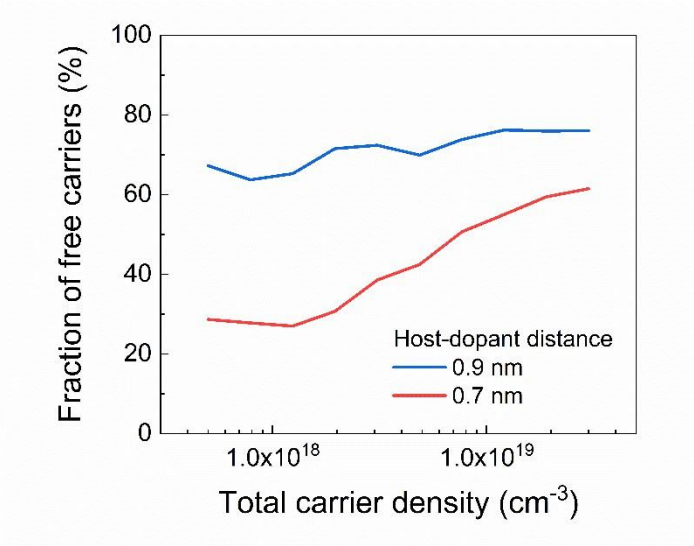

Figure S15. The kinetic Monte Carlo simulations of the steady-state transport of polarons in disordered and doped organic semiconductor: the simulated plots of fraction of charges localized away from the dopant as a function of the total charge density.

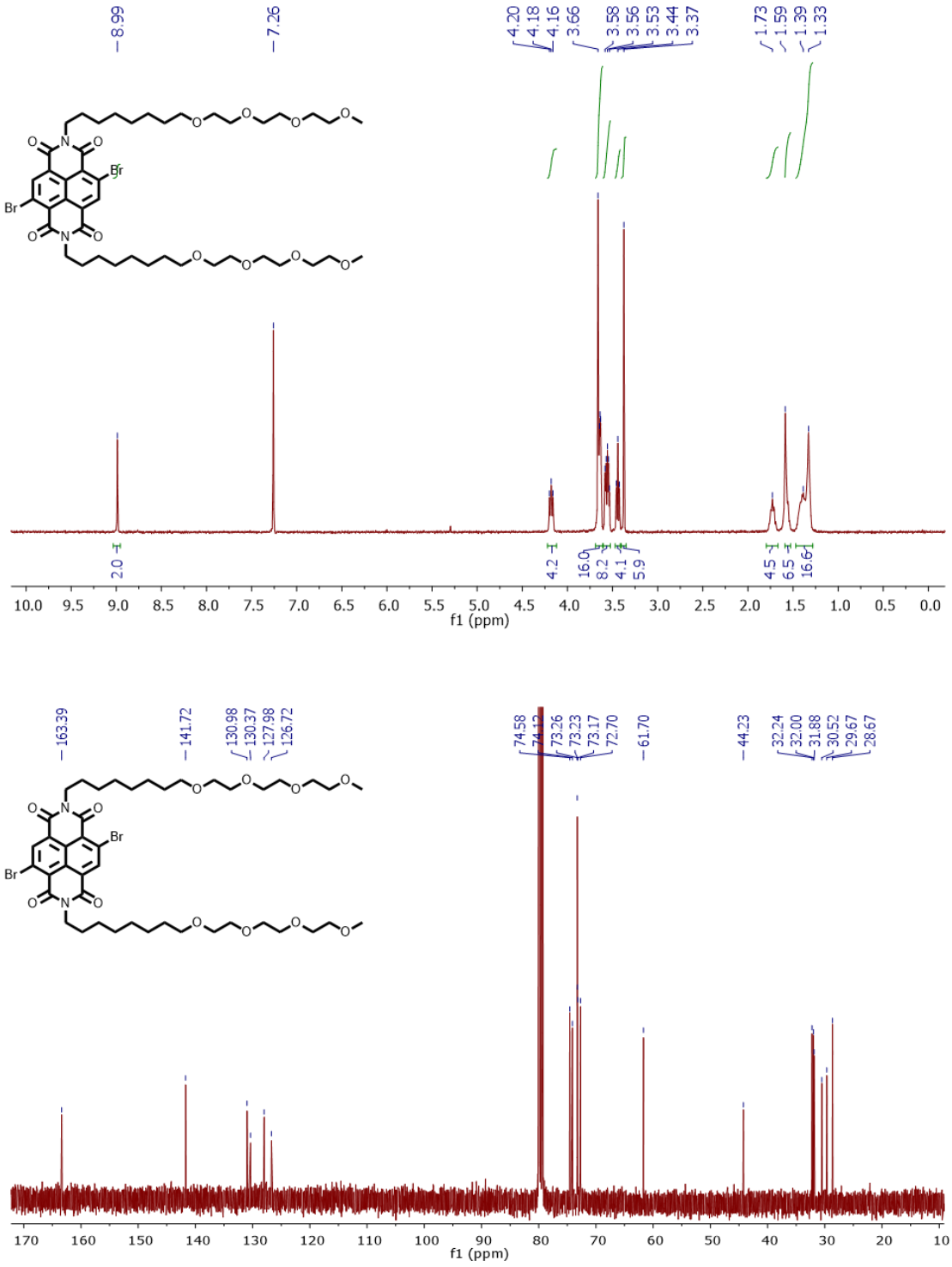

Figure S16. ^{1}H NMR (top) and ^{13}C NMR (bottom) spectra of monomer **NDI2C8TEG.**

NDI2C8TEG

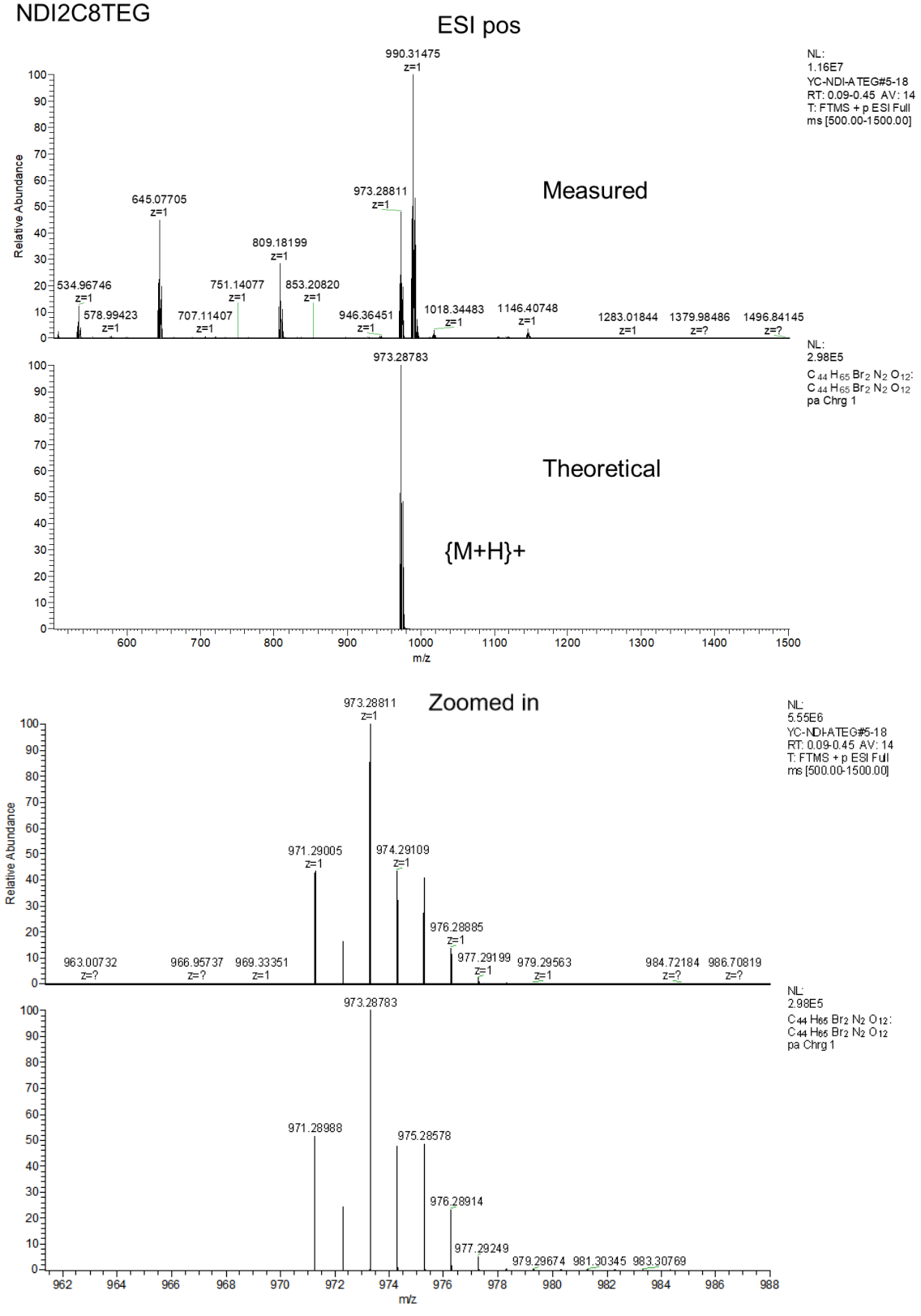
ESI pos
990.31475
z=1
NL:
1.16E7
YC-NDI-ATEG#5-18
RT: 0.09-0.45 AV: 14
T: FTMS + p ESI Full
ms [500.00-1500.00]
Measured
973.28811
z=1
645.07705
z=1
809.18199
z=1
534.96746
z=1
751.14077
z=1
853.20820
z=1
578.99423
z=1
707.11407
z=1
946.36451
z=1
1018.34483
z=1
1146.40748
z=1
1283.01844
z=1
1379.98486
z=?
1496.84145
z=?
Relative Abundance
973.28783
NL:
2.98E5
C44 H65 Br2 N2 O12:
C44 H65 Br2 N2 O12
pa Chrg 1
Theoretical
{M+H}+
m/z
Zoomed in
973.28811
z=1
NL:
5.55E6
YC-NDI-ATEG#5-18
RT: 0.09-0.45 AV: 14
T: FTMS + p ESI Full
ms [500.00-1500.00]
971.29005
z=1
974.29109
z=1
976.28885
z=1
977.29199
z=1
963.00732
z=?
966.95737
z=?
969.33351
z=1
979.29563
z=1
984.72184
z=?
986.70819
z=?
Relative Abundance
973.28783
NL:
2.98E5
C44 H65 Br2 N2 O12:
C44 H65 Br2 N2 O12
pa Chrg 1
971.28988
975.28578
976.28914
977.29249
979.29674
981.30345
983.30769
m/z

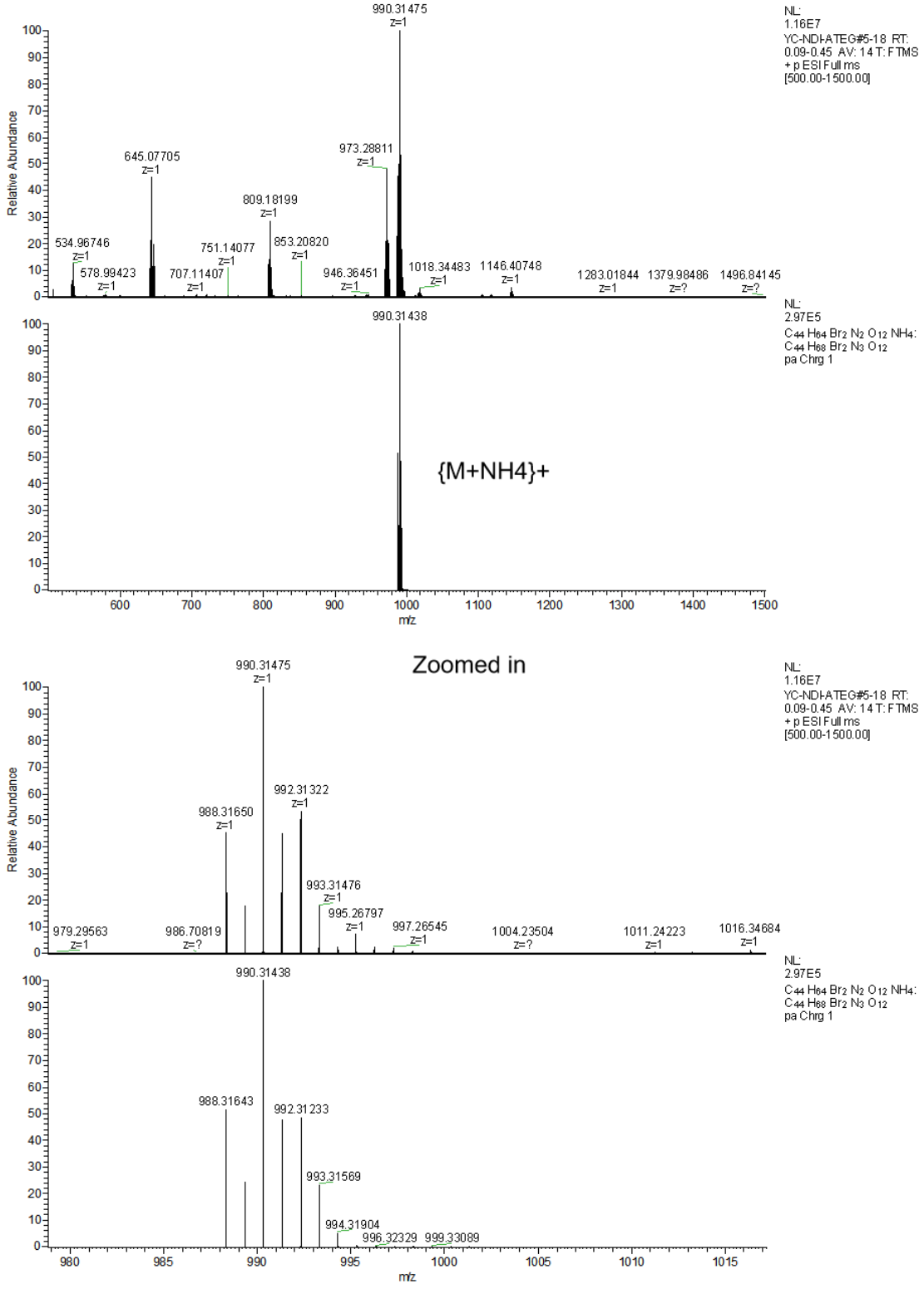

Figure S17. HRMS spectra of monomer **NDI2C8TEG**

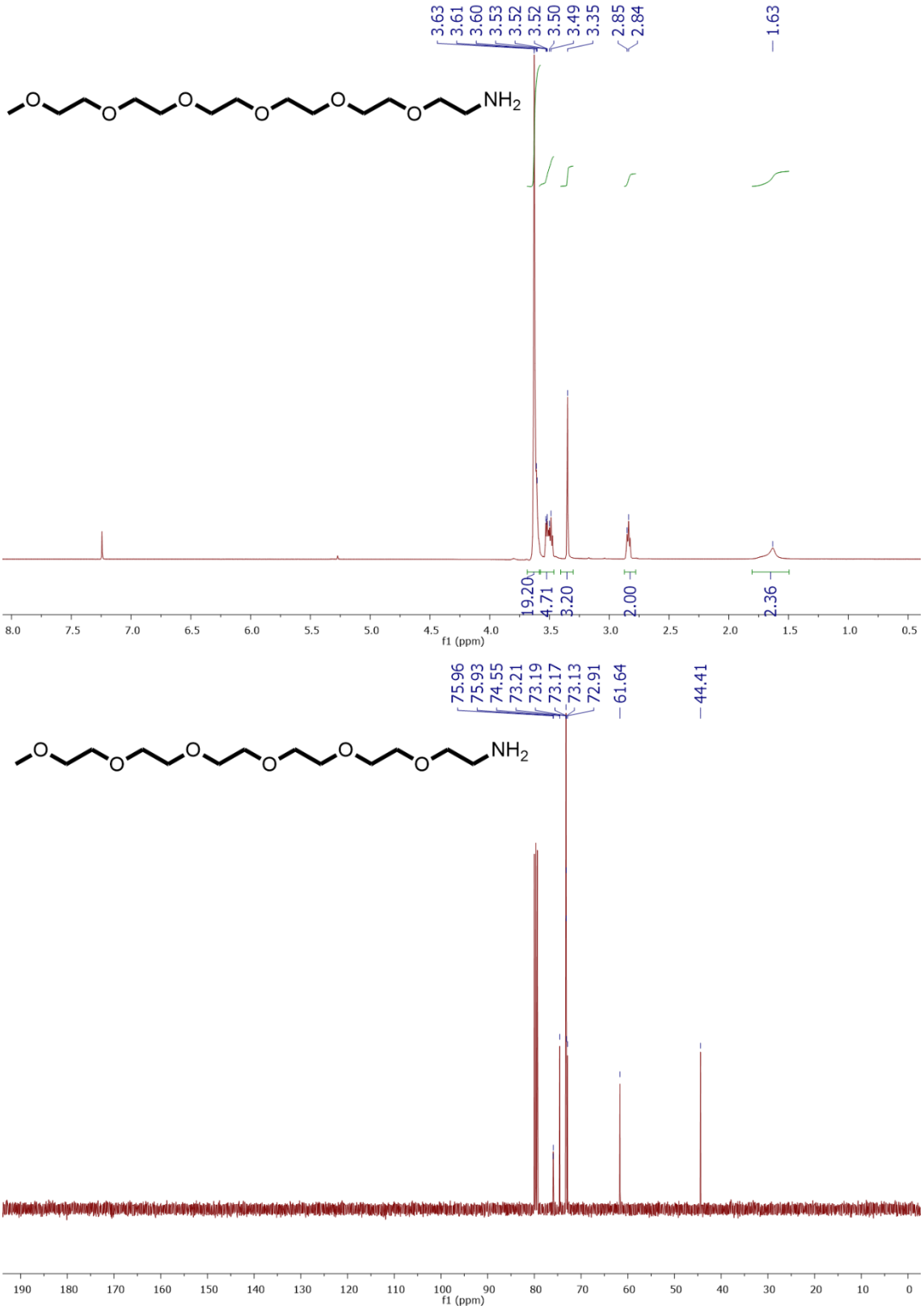

Figure S18. ^{1}H NMR (top) and ^{13}C NMR (bottom) spectra of monomer **HexEGNH2.**

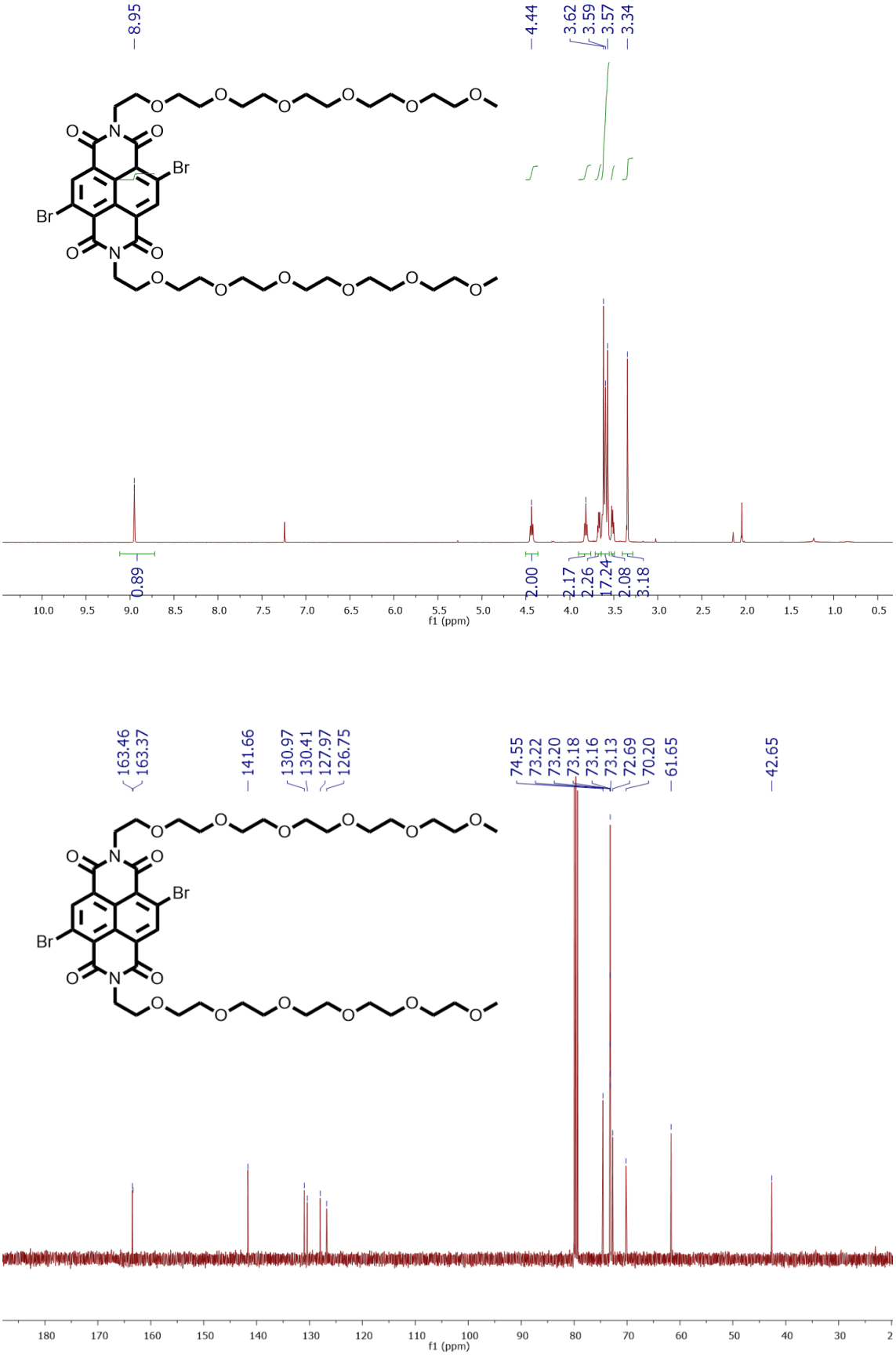

Figure S19. ^{1}H NMR (top) and ^{13}C NMR (bottom) spectra of monomer **NDI2HexEG.**

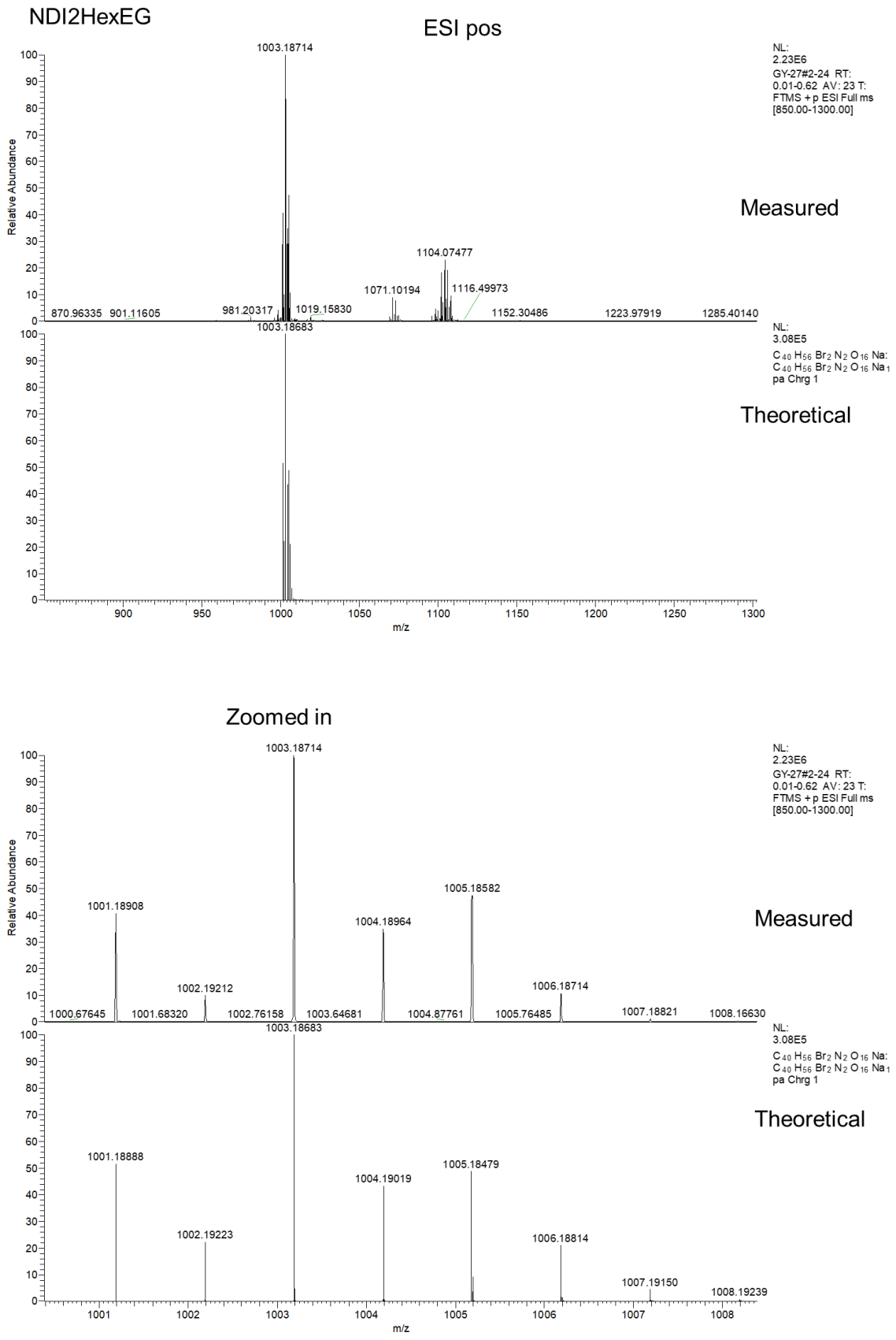

Figure S20. HRMS spectra of monomer **NDI2HexEG.**

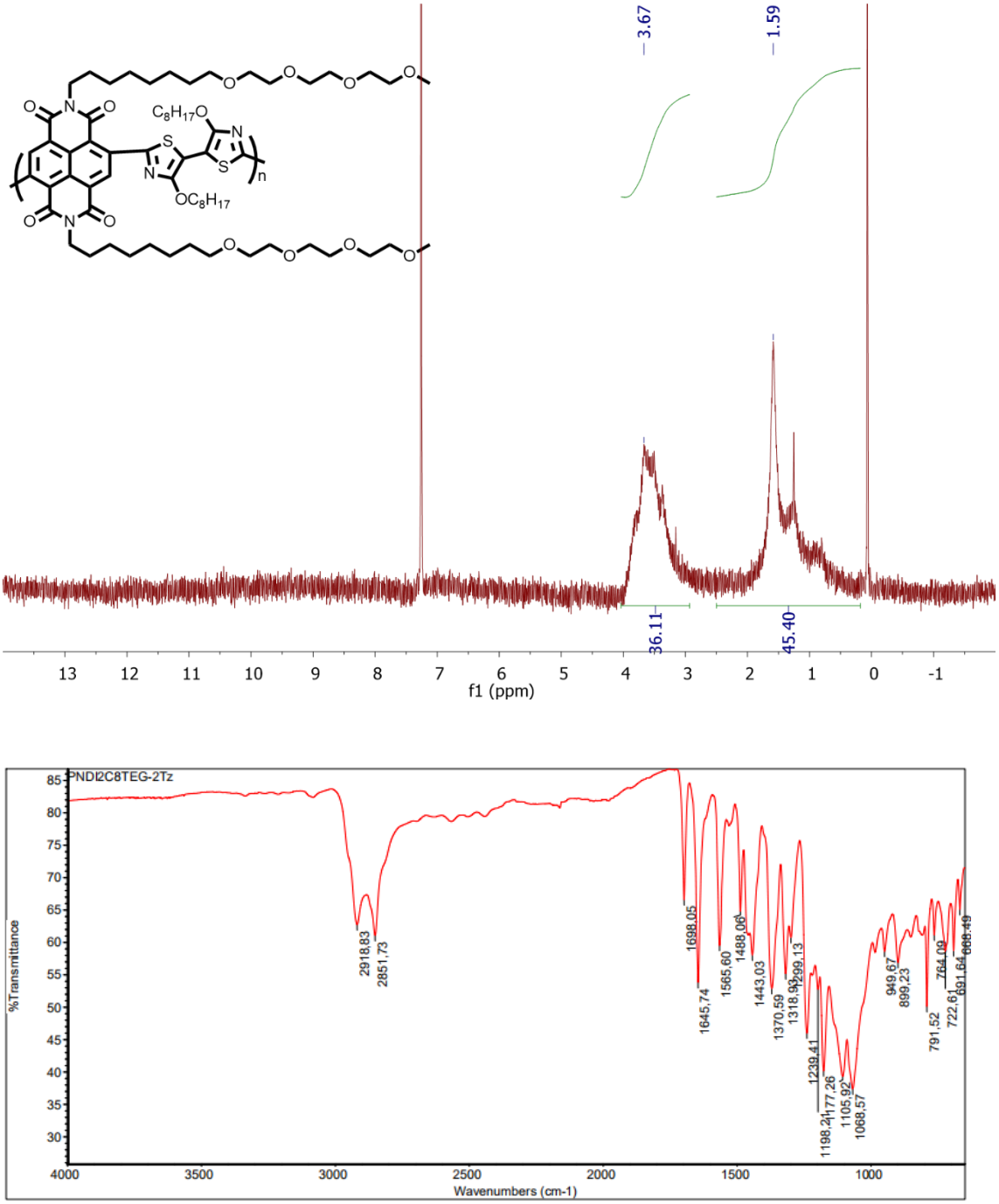

Figure S21. [1]HNMR (top) and IR (bottom) spectra of PNDI2C8TEG-2Tz.

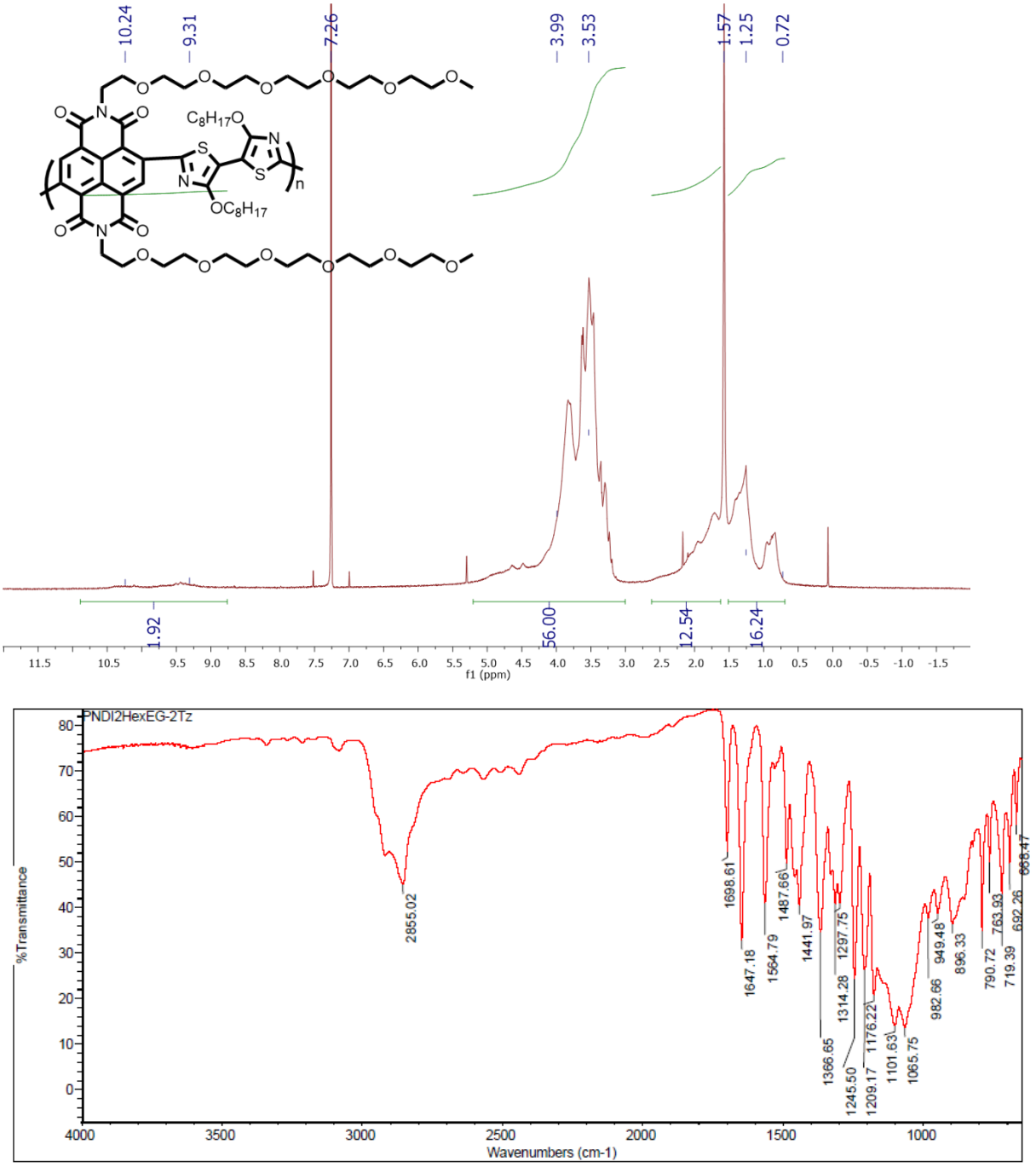

Figure S22. ^{1}HNMR (top) and IR (bottom) spectra of PNDI2HexEG-2Tz.

References

[S1] R. Kim, B. Kang, D. H. Sin, H. H. Choi, S. Kwon, Y. Kim, K. Cho. *Chem. Commun.*, 2015,**51**, 1524-1527.

[S2] J. Liu, G. Ye, B. van der Zee, J. Dong, X. Qiu, Y. Liu, G. Portale, R. C. Chiechi, and L. J. A. Koster. *Adv. Mater.* 2018, **30**, 1804290.

[S3] D. Komáromy, M. C. A. Stuart, G. M. Santiago, M. Tezcan, V. V. Krasnikov, and Sijbren Otto. *J. Am. Chem. Soc.* 2017 **139**, 6234-6241.

[S4] H. F. Higginbotham, S. Maniam, S. J. Langford, T. D.M. Bell, *Dyes and Pigments* 2015, **112**, 290.

[S5] A. Giovannitti, R. B. Rashid, Q. Thiburce, B. D. Paulsen, C. Cendra, K. Thorley, D. Moia, J. T.r Mefford, D. Hanifi, D. Weiyuan, M. Moser, A. Salleo, J. Nelson, I. McCulloch, and J. Rivnay. *Adv. Mater.* 2020, 1908047.

[S6] J. Liu, L. Qiu, G. Portale, M. Koopmans, G. ten Brink, J. C. Hummelen, L. J. A. Koster, *Adv. Mater.* **2017**, *29* (36), 1701641.

[S7] D. Venkateshvaran, M. Nikolka, A. Sadhanala, V. Lemaur,; M. Zelazny, M. Kepa, M. Hurhangee, A. J. Kronemeijer, V. Pecunia, I. Nasrallah, I. Romanov, K. Broch, I. McCulloch, D. Emin, Y. Olivier, J. Cornil, D. Beljonne, H. Sirringhaus, *Nature* **2014**, *515*, 384.

[S8] S. Sami, M.F.S.J. Menger, S. Faraji, R. Broer, R.W.A. Havenith, Q-Force: Quantum mechanically augmented molecular force fields. https://github.com/selimsami/qforce

[S9] S. Sami, R. Alessandri, R. Broer, R.W.A. Havenith, *ACS Appl. Mater. Interfaces* **2020**, *12*, 17783.

[S10] H. J. C. Berendsen, J. P. M. Postma, W. F. van Gunsteren, A. DiNola, J. R. Haak, *J. Chem. Phys.* **1984**, *81*, 3684.

[S11] T. Darden, D. York, L. Pedersen, *J. Chem. Phys.* **1993**, *98*, 10089.

[S12] M. J. Abraham, T. Murtola, R. Schulz, S. Páll, J. C.Smith, B. Hess, E. Lindahl, *SoftwareX* **2015**, *1*, 19.

[S13] R. a. Schlitz, F. G. Brunetti, A. M. Glaudell, P. L. Miller, M. a. Brady, C. J. Takacs, C. J. Hawker, M. L. Chabinyc, Adv. Mater. 2014, 26, 2825.

[S14] J. Liu, L. Qiu, R. Alessandri, X. Qiu, G. Portale, J. Dong, W. Talsma, G. Ye, A. A. Sengrian, P. C. T. Souza, M. A. Loi, R. C. Chiechi, S. J. Marrink, J. C. Hummelen, L. J. A. Koster, Adv. Mater. 2018, 30, 1704630.

[S15] D. Kiefer, A. Giovannitti, H. Sun, T. Biskup, A. Hofmann, M. Koopmans, C. Cendra, S. Weber, L. J. Anton Koster, E. Olsson, J. Rivnay, S. Fabiano, I. McCulloch, C. Müller, ACS Energy Lett. 2018, 3, 278.

[S16] S. Wang, H. Sun, T. Erdmann, G. Wang, D. Fazzi, U. Lappan, Y. Puttisong, Z. Chen, M. Berggren, X. Crispin, A. Kiriy, B. Voit, T. J. Marks, S. Fabiano, A. Facchetti, Adv. Mater. 2018, 30, 1801898.

[S17] Y. Wang, M. Nakano, T. Michinobu, Y. Kiyota, T. Mori, K. Takimiya, Macromolecules 2017, 50, 857.

[S18] Y. H. Shin, H. Komber, D. Caiola, M. Cassinelli, H. Sun, D. Stegerer, M. Schreiter, K. Horatz, F. Lissel, X. Jiao, C. R. McNeill, S. Cimò, C. Bertarelli, S. Fabiano, M. Caironi, M. Sommer, Macromolecules 2020, 53, 5158.

[S19] S. Wang, H. Sun, U. Ail, M. Vagin, P. O. Å. Persson, J. W. Andreasen, W. Thiel, M. Berggren, X. Crispin, D. Fazzi, S. Fabiano, Adv. Mater. 2016, 28, 10764.

[S20] K. Shi, F. Zhang, C.-A. Di, T.-W. Yan, Y. Zou, X. Zhou, D. Zhu, J.-Y. Wang, J. Pei, J. Am. Chem. Soc. 2015, 2.

[S21] X. Zhao, D. Madan, Y. Cheng, J. Zhou, H. Li, S. M. Thon, A. E. Bragg, M. E. DeCoster, P. E. Hopkins, H. E. Katz, Adv. Mater. 2017, 29, 1606928.

[S22] X. Yan, M. Xiong, J.-T. Li, S. Zhang, Z. Ahmad, Y. Lu, Z.-Y. Wang, Z.-F. Yao, J.-Y. Wang, X. Gu, T. Lei, J. Am. Chem. Soc. 2019, 141, 20215.

[S23] Y. Wang, K. Takimiya, Adv. Mater. 2020, 2002060.

[S24] C.-Y. Yang, Y.-F. Ding, D. Huang, J. Wang, Z.-F. Yao, C.-X. Huang, Y. Lu, H.-I. Un, F.-D. Zhuang, J.-H. Dou, C. Di, D. Zhu, J.-Y. Wang, T. Lei, J. Pei, Nat. Commun. 2020, 11, 3292.

[S25] A. F. Voter, Introduction to the kinetic Monte Carlo method. In Radiation effects in solids, Springer, Dordrecht **2007**.

[S26] M. C. Heiber, *J. Open Source Software* **2020** 5, 2307.
https://github.com/MikeHeiber/Excimontec

[S27] G. Kim, , K. P. Pipe, *Physical Review B*, **2012**, *86*, 085208.

[S28] F. Liu, H. van Eersel , B. Xu, J. G. Wilbers, M. P. de Jong, W. G. van der Wiel, P. A. Bobbert, R. Coehoorn, *Physical Review B*, **2017**, **96**, 205203.